

FACULTY
OF MATHEMATICS
AND PHYSICS
Charles University

MASTER THESIS

Bc. Martin Hronek

Inverse physics-based modeling of the 2016 Mw 6.1 Tottori earthquake

Department of Geophysics

Supervisor of the master thesis: Prof. RNDr. František Gallovič, Ph.D.

Study programme: Geophysics and Physics of the Planets

Prague 2025

I declare that I carried out this master thesis on my own, and only with the cited sources, literature and other professional sources. I understand that my work relates to the rights and obligations under the Act No. 121/2000 Sb., the Copyright Act, as amended, in particular the fact that the Charles University has the right to conclude a license agreement on the use of this work as a school work pursuant to Section 60 subsection 1 of the Copyright Act.

In ..... date ....

Author's signature

I would like to express my sincere gratitude to my thesis supervisor, Prof. František Gallovič, for his collaboration throughout this work, for his patience, valuable advice, and insightful comments. I am also deeply grateful for the opportunity to work on such a meaningful and engaging research topic, and for the opportunity to present my work at two scientific conferences during my Master's studies.

I am also grateful to Prof. Jiří Zahradník, DrSc., Dr. Ľubica Valentová Krišková, Dr. Jan Premus, Dr. Vladimír Plicka, and Assoc. Prof. Johana Brokešová, CSc., for introducing me to the beauty of seismology. My thanks also go to all the other inspiring teachers who dedicated their time and sparked my enthusiasm for the study of geophysics. I am truly grateful to everyone at the Department of Geophysics for creating such a welcoming and supportive environment.

I would like to thank all my friends and fellow students for the many wonderful moments we shared and for their encouragement along the way. Special thanks go to the PC lab community, The Seven Illusions of Hanka Čížková, for the friendly and pleasant atmosphere.

Finally, my deepest thanks go to my family for their unwavering support. I would particularly like to express my heartfelt gratitude to my recently deceased grandfather, who always supported me in my studies.

Title: Inverse physics-based modeling of the 2016 Mw 6.1 Tottori earthquake

Author: Bc. Martin Hronek

Department: Department of Geophysics

Supervisor: Prof. RNDr. František Gallovič, Ph.D., Department of Geophysics

Abstract: The 2016 Mw 6.2 left-lateral strike-slip Tottori earthquake occurred in the central part of the Tottori Prefecture in the Chugoku region in western Japan. Published rupture models inferred either from geodetic or seismic data exhibit significant discrepancies. In this study, we perform a so-far missing dynamic rupture simulation to improve the understanding of the event. We utilize the 3D finite-difference staggered grid code FD3D_TSN to simulate the dynamic rupture propagation assuming the classic linear slip-weakening friction law on a planar vertical fault. Synthetic seismograms are calculated using the representation theorem by convolving the obtained slip rates with Green's functions precalculated in 1D velocity models acquired for each station from a 3D model.
We utilize the fd3d_tsn_pt code to perform a dynamic source inversion with spatially variable prestress and friction parameters, formulated in a Bayesian framework, employing the Parallel Tempering MCMC approach to sample the posterior distribution of the model parameters. We use local low-frequency seismic waveforms (up to 0.6-1.2 Hz) and GNSS static coseismic displacements. We obtain posterior model samples with complex rupture propagation, discuss the inferred heterogeneous rupture parameters in a statistical sense, and compare them with previously published models. We evaluate correlations and trade-offs among kinematic and dynamic rupture parameters. We find that the slip-weakening distance increases in average linearly with distance from the hypocenter, which can be interpreted as an apparent feature substituting the effect of (unmodeled) significant off-fault yielding.

Keywords: Dynamic Seismic Source Inversion, Dynamic Rupture Propagation Simulation, Earthquake Modeling, Bayesian MCMC Inverse Problem, The 2016 Mw 6.2 Tottori earthquake

Contents

1 Introduction **6**
- 1.1 Central Tottori 2016 earthquake . . . 6
- 1.2 Region . . . 6
- 1.3 Published papers . . . 8
- 1.4 Motivation and content of the Thesis . . . 11

2 Theoretical part **12**
- 2.1 Dynamic rupture simulations . . . 12
  - 2.1.1 Elastodynamic equation and its solution . . . 12
  - 2.1.2 Dynamic representation of an earthquake source . . . 13
  - 2.1.3 Friction law . . . 14
  - 2.1.4 Outer boundary conditions . . . 16
  - 2.1.5 Overview of rupture parameters . . . 17
- 2.2 Synthetic waveforms and static displacements . . . 19
  - 2.2.1 Synthetic waveforms . . . 19
  - 2.2.2 Static displacements . . . 20
- 2.3 Inverse problem . . . 21
  - 2.3.1 Formulation of the inverse problem . . . 21
  - 2.3.2 Algorithm of the inverse problem . . . 23

3 Data and method **25**
- 3.1 Data, velocity model and aftershocks . . . 25
- 3.2 Methods . . . 25
  - 3.2.1 Forward problem . . . 28
  - 3.2.2 Model parametrization and frictional law . . . 29
  - 3.2.3 Inverse problem . . . 29

4 Results **32**
- 4.1 Maximum a posteriori model . . . 32
- 4.2 Ensemble models . . . 38

5 Discussion **44**
- 5.1 Comparison to published papers . . . 44
- 5.2 Variability of rupture parameters within the ensemble . . . 45
- 5.3 Slip-weakening distance vs distance from the nucleation . . . 47
- 5.4 Parameters correlations, and trade-offs . . . 50
- 5.5 Foreshocks and aftershocks . . . 53

Conclusion **54**

Bibliography **55**

1 Introduction

1.1 Central Tottori 2016 earthquake

On 21 October 2016, a strong earthquake with a moment magnitude of Mw 6.2 occurred on Japan's largest island, Honshu, in the central part of the local Tottori Prefecture in the Chugoku region. According to the Japan Meteorological Agency (JMA) magnitude scale, the magnitude was 6.6 (MJMA). Moment tensor solutions from the F-net suggest that this was a left-lateral strike-slip event in shallow crust with a strike of 162°, dip of 80°, and rake of 9° (Earth Science and Resilience, 2019). The location of the nucleation point, determined by the Hi-net seismogram network, is 35.3806°N, 133.8545°E, at a depth of 11.58 km.

The mainshock caused strong ground motions with a maximum PGA of 1.4 gal and a JMA intensity of 5.8 (see Figure 1.1). According to Reuters (2016), fortunately, there were no fatalities, but some people were injured. Observed damage included toppled gravestones, fallen roof tiles, items falling from shelves, some damage to buildings, and at least one building collapsed.

The mainshock itself was preceded by 70 foreshocks over 12 hours, the largest was Mw 4.2, and followed by more than ten thousand aftershocks over the following 10 days; the largest was Mw 5.0, 46 minutes after the mainshock (Ross et al., 2018); see Figure 1.2. Events at depths greater than 8 km are concentrated on the fault or subparallel to the strike, whereas shallow seismicity is mostly off-fault. In Figure 1.3, we see that the earthquake triggered significant off-fault seismicity as far as 15-20 km from the fault.

1.2 Region

The Tottori 2016 earthquake occurred within the right-lateral San-in shear zone (SZZ) (Nishimura and Takada, 2017), which is part of the larger right-lateral North Chugoku shear zone (NCSZ) (Gutscher and Lallemand, 1999); see Figure 1.4.

According to Nishimura and Takada (2017), the SZZ is an approximately 50 km wide concentrated deformation zone that can be modeled by a deep creep on a vertical strike-slip fault with a creep rate of about 5 mm/year. They suggest that the SZZ is a young and still developing shear zone, which probably accommodates a part of the relative plate motion of the subducting Philippine Sea plate and the overriding Amurian plate, and the seismicity is attributed to conjugate Riedel shears.

The region has a rich history of diverse seismic activity, including seismic swarms, deep low-frequency earthquakes, and a large number of moderate to large earthquakes over the past century, despite a small amount of accumulated stress (Ross et al., 2018). Several large crustal earthquakes have struck the Tottori prefecture during the last century; see Figure 1.5. The most damaging earthquake, with a Mw magnitude of 7.0, occurred in 1943 east of the 2016 hypocenter. This event was disastrous for Tottori City, where a large number of buildings were damaged, and unfortunately, there were also fatalities. Less destructive were the 1983 6.2 Mw earthquake in the central part of Tottori Prefecture and the 2000

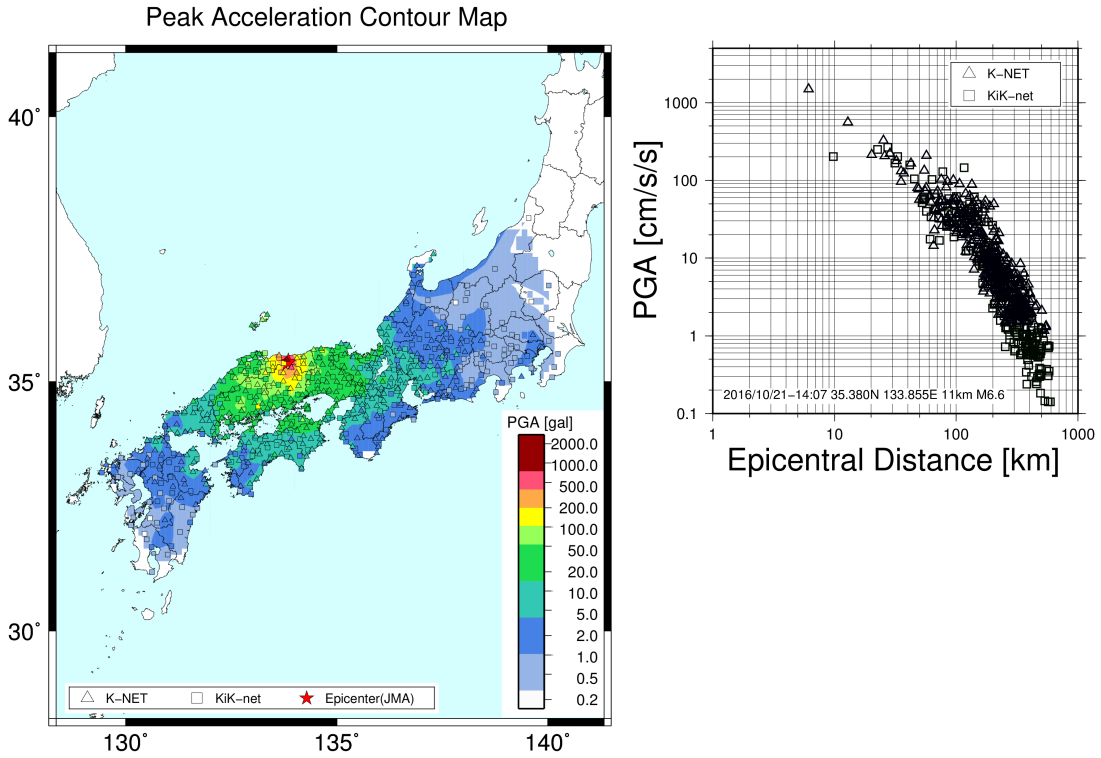


Figure 1.1 Map of peak ground acceleration (PGA) caused by the mainshock on the left and the decay of PGA with epicentral distance on the right, adapted from the NIED (Earth Science and Resilience, 2019).

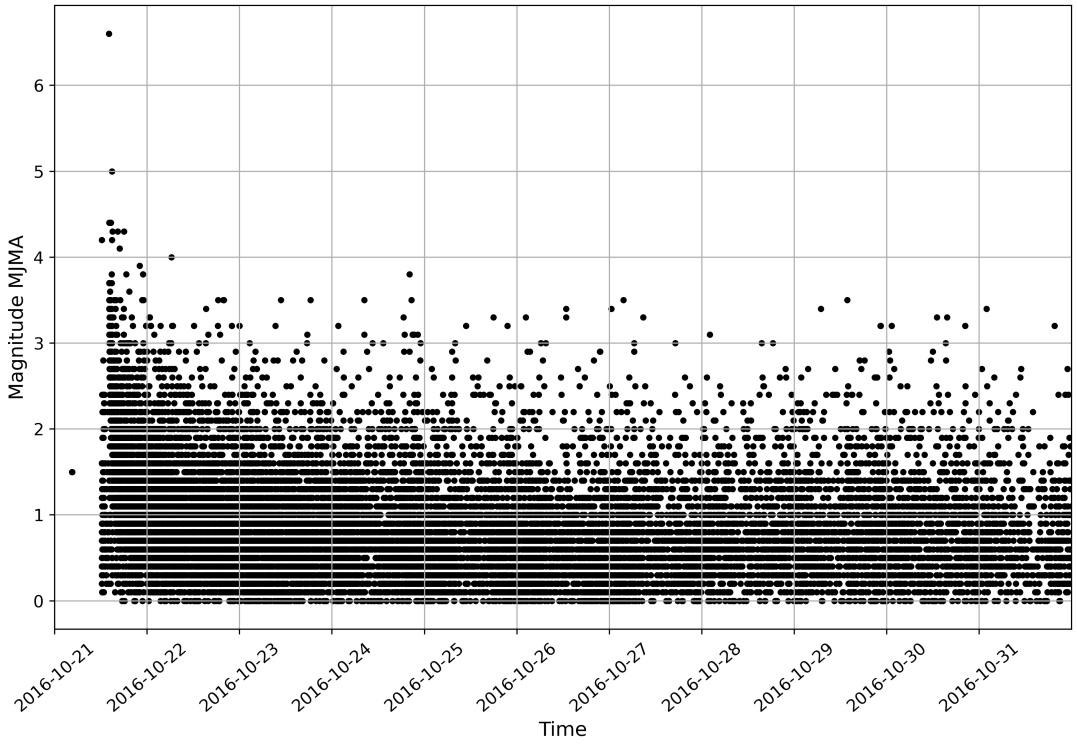


Figure 1.2 Magnitude distributions of foreshocks and aftershocks in time. Data downloaded from Ross et al. (2018).

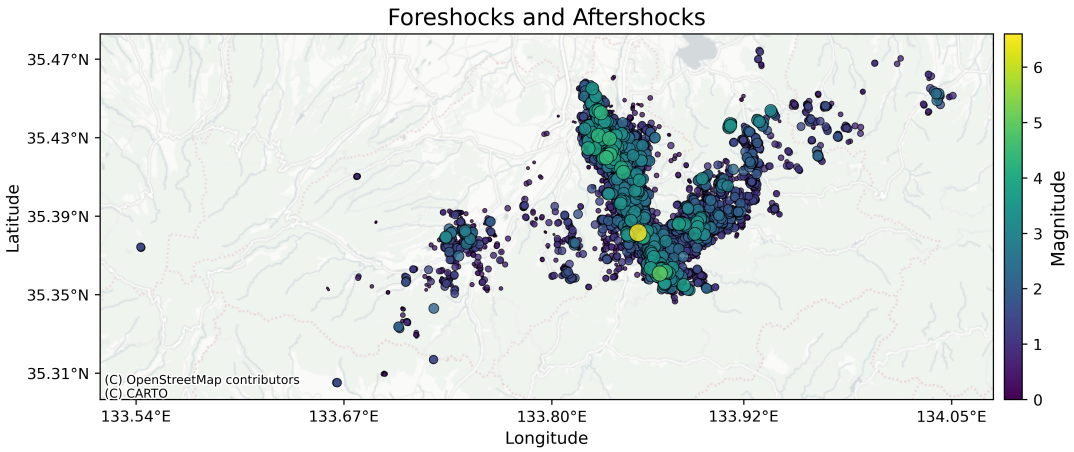


Figure 1.3 Map of foreshocks and aftershocks. Data downloaded from Ross et al. (2018).

7.3 Mw earthquake in the western part of Tottori. Both the 2000 and 2016 events triggered significant seismicity far away from their ruptures.

1.3 Published papers

Here, we present an overview of the slip distribution from published kinematic source inversions.

Ross et al. (2018) inverted apparent source-time functions obtained by an empirical Green's function deconvolution method. They observed a fairly deep and confined rupture with high slip values. The exact slip values depend on the assumed rupture velocity and regularization. Their rupture is circular with an area of 16 km^2, located approximately around the hypocenter (11 km along the strike and 4.5 km in the up-dip direction) with an average slip of 3.2 m and a maximum 5.3 m. According to their conclusion, the rupture probably does not extend above 8 km.

According to the multiple-time window finite-fault kinematic strong-motion waveform inversion (0.1-1.0 Hz) using the theoretical Green's function from Kubo et al. (2017), there are two main rupture asperities. The first one (0-3 s) goes from the hypocenter mainly in the vertical direction to the shallower depths with a maximum slip of 0.6 m. The second one (3-5 s) in the NNW direction from the hypocenter is smaller, with a maximum slip of 0.5 m. The released seismic moment from the second asperity is about five times smaller than that from the first, and its contribution to the waveforms is smaller. However, the second slip region is necessary to fit the later parts of the waveforms at some stations.

The inversion of coseismic and postseismic slip using GNSS and InSAR data from Meneses-Gutierrez et al. (2019) reveals a large coseismic slip region in the northwest direction of the hypocenter up to a depth of approximately 1 km, without reaching the surface, with a maximum slip of 1.28 m and with an error range

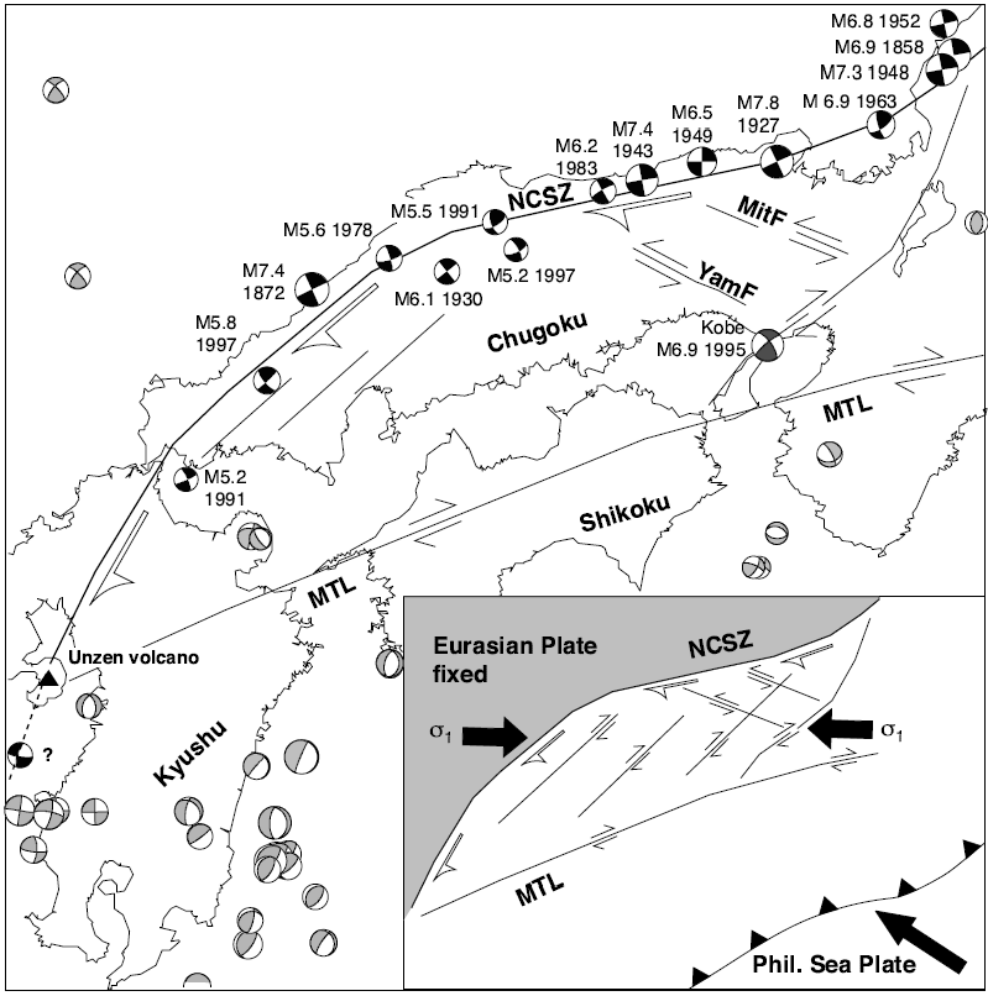


Figure 1.4 Map of selected shallow (depth < 70 km) and M > 5 earthquakes in SW Japan with focal mechanism. Events related to the North Chugoku shear zone (NCSZ) are shown in black, others are gray. The figure is adopted from Gutscher and Lallemand (1999).

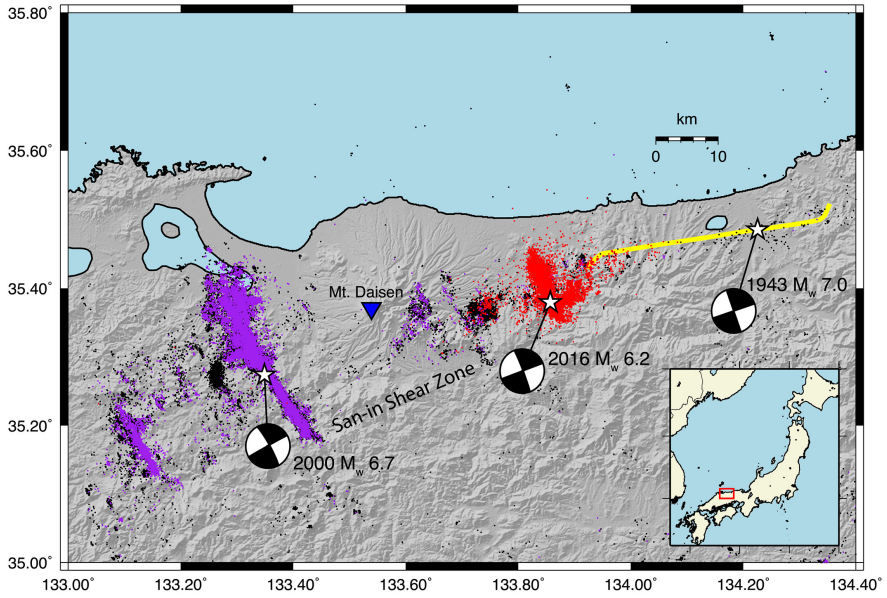


Figure 1.5 Map of recent large earthquakes in the Tottori prefecture. The figure is reproduced from Ross et al. (2018). White stars are the hypocenters. The red and purple dots indicate the locations of the foreshocks and aftershocks projected onto the surfaces of the 2016 and 2000 earthquakes, respectively. The yellow curve is a surface projection of the 1943 earthquake fault. Blue triangle is a dormant stratovolcano Mount Daisen.

$5 - 35$ cm. According to their synthetic test, a shallow slip is necessary to fit the geodetic observations, even though the primary slip occurs between 4 and 10 km deep. In contrast, their postseismic model shows a large, shallow afterslip area at depths from 0 to 4 km.

Amey et al. (2019) performed a transdimensional Bayesian geodetic slip inversion constrained by InSAR and GNSS observations, and applied von Karman regularization to capture the fractal nature of slip. Their results indicate a large smeared slip region with a peak slip of 1.3 m at a depth of 6 km. The slip distribution extends mainly from depths of around 1.5 km to approximately 10 km, with minor slips at deeper parts.

Shibata and Aso (2025) used radiation-corrected empirical Green's functions in kinematic strong-motion (0.1-1.0 Hz) waveform inversion. They obtained the largest slip in the small region around the hypocenter, and moderate slip up to the shallower parts with a large variety between models due to the relatively small number of stations (8) suitable for this EGF method.

1.4 Motivation and content of the Thesis

Published kinematic rupture models inferred either from geodetic or seismic data exhibit significant discrepancies. To better understand this event, we performed a so-far missing dynamic rupture simulation and followed with a dynamic source inversion considering the slip-weakening friction law with spatially heterogeneous prestress and friction parameters distributions on the fault.

Firstly, as part of my Bachelor thesis (Hronek, 2023), we performed a parametric study considering simple elliptical distributions of prestress and slip-weakening friction law parameters using low-frequency seismic data to find an optimal distribution of the dynamic parameters that best fits the observed seismograms. We assumed a deep elliptical rupture following the results of Ross et al. (2018). We obtained various models of possible slip evolution on the fault; however, the fit of the seismograms, especially at very close distances, was not satisfactory. Thus, we concluded that a more complex inhomogeneous parameter distribution on the fault with perhaps shallower slip was necessary. Here, we proceed with dynamic source inversion, which will be described in the following.

The thesis is organized as follows. In Subchapter 2.1, we describe the basic theoretical background of dynamic earthquake modeling, focusing on the method used in this research. We introduce the elastodynamic equation and its solution, as well as the dynamic representation of an earthquake source, friction laws, boundary conditions, and an overview of rupture parameters.

In Subchapter 2.2, we introduce the Green tensor and the representation theorem. We also describe how to calculate synthetic waveforms and static displacements from the slip rate function distribution on the fault, which is the result of a dynamic rupture simulation.

In the following subchapter 2.3, we formulate and explain our inverse problem. We introduce the misfit function, the posterior probability density function, acceptance rules, etc.

In subchapter 3.1, we present the seismic and geodetic data used in this study and describe the applied processing methods. Then, in subchapter 3.2, we describe the method, which we have divided into three parts: the forward problem, model parametrization and frictional law, and the inverse problem. We also briefly summarize the overall workflow and inversion strategy.

In Chapter 4, we present the maximum a posteriori model, and then discuss the averaged properties of the inferred ensemble models.

In Chapter 5, we compare our results to those in published papers. Then, we discuss the variability of rupture parameters within the ensemble. We also evaluate the correlations and trade-offs between these parameters. Additionally, we examine the relationship between aftershocks and source parameters. Finally, we examine the linear increase in slip-weakening distance and fracture energy density with respect to nucleation distance.

The conclusion is found in Chapter 5.5.

2 Theoretical part

2.1 Dynamic rupture simulations

Dynamic rupture models solve the elastodynamic equation with the constitutive friction laws for the surface forces acting on the fault, and thus provide insight into the evolution of slip and stresses on tectonic faults. They enable us to study the seismic source parameters that influence the rupture process and perform simulations of the possible evolution of the earthquake rupture propagation. Furthermore, they allow us to build a database of synthetic dynamic rupture scenarios, which can be used for ground motion evaluation and thus for seismic hazard assessment.

The following section describes the basic theoretical background of dynamic earthquake modeling, with a focus on the method used in this study.

2.1.1 Elastodynamic equation and its solution

Dynamic rupture simulation codes are based on the solution of the elastodynamic equation, which in the classical velocity-stress formulation reads (see Moczo et al. (2007)):

$$\rho \frac{\partial v_i}{\partial t} = \sigma_{ij,j}, \tag{2.1}$$

$$\frac{\partial \sigma_{ij}}{\partial t} = c_{ijkl} v_{k,l}, \tag{2.2}$$

where the first equation represents the conservation of momentum in differential form, and the second is Hooke's law. Here ρ is the density of the elastic medium, v_i denotes the i-th component of velocity (the time derivative of the displacement field), t is time, σ_{ij} denotes the stress tensor and c_{ijkl} is the elastic moduli tensor. The Einstein summation convention is used. We assume an isotropic medium with the elastic modulus tensor in the form:

$$c_{ijkl} = \lambda \delta_{ij} \delta_{kl} + \mu(\delta_{ij}\delta_{jl} + \delta_{il}\delta_{jk}), \tag{2.3}$$

where λ a μ are the so-called Lame's coefficients.

Solving the elastodynamic equation requires advanced numerical techniques, such as the finite-difference method (e.g., FD3D_TSN by Premus et al. (2020), AWP-ODC by Roten et al. (2016), CG-FDM by Zhang et al. (2014)), finite-element (e.g., FaultMod by Barall (2009)), spectral-element (e.g., SEM2DPACK by Ampuero et al. (2024)), or discontinuous Galerkin (e.g., SeisSol by Uphoff et al. (2024)). For a list of other codes, see Table 1 in R. A. Harris et al. (2018).

Here, equations (2.1) and (2.2) are solved using the finite difference (FD) method. The numerical calculations are performed on a regular grid in the Cartesian coordinate system with time as the fourth dimension, and material parameters are assumed to be constant within a grid cell.

The FD method uses nine fourth-order FD operators to discretize $\boldsymbol{v}$ and $\boldsymbol{\sigma}$ on a regular 3D staggered grid introduced in Graves (1996), where the velocity

$\boldsymbol{v}$ and the stress tensor $\boldsymbol{\sigma}$ are not calculated at the same points on the grid, but are regularly offset in both space and time with respect to the discretization of the equations; see also Premus et al. (2020). Bilinear interpolation is therefore required to apply the friction law.

2.1.2 Dynamic representation of an earthquake source

In dynamic rupture simulation, an earthquake source is represented as a spontaneous shear rupture propagation on the fault. The fault is a frictional plane interface between two elastic half-spaces, here denoted "+" and "-". This section 2.1.2 describes the basic formulation of the problem and follows Moczo et al. (2007).

The slip $\boldsymbol{s}$ is defined as the discontinuity of the displacement vector $\boldsymbol{u}$ across the fault, and the slip rate $\dot{\boldsymbol{s}}$ is its time derivative, i.e., the particle velocity vector discontinuity across the fault:

$$\boldsymbol{s}(\boldsymbol{x}, t) = \boldsymbol{u}^{+}(\boldsymbol{x}^{+}, t) - \boldsymbol{u}^{-}(\boldsymbol{x}^{-}, t), \tag{2.4}$$

$$\dot{\boldsymbol{s}}(\boldsymbol{x}, t) = \dot{\boldsymbol{u}}^{+}(\boldsymbol{x}^{+}, t) - \dot{\boldsymbol{u}}^{-}(\boldsymbol{x}^{-}, t). \tag{2.5}$$

Note that the slip represents the relative motion of the "+" side relative to the "-" side of the fault.

In the case of a shear rupture, the normal components (index n) of the displacement vector and the velocity vector are assumed to be continuous at a given location on the fault surface, and, conversely, their shear components (index sh) are assumed to be discontinuous:

$$[u_n]^{\pm} = 0,\ [v_n]^{\pm} = 0, \tag{2.6}$$

$$[u_{sh}]^{\pm} \neq 0,\ [v_{sh}]^{\pm} \neq 0. \tag{2.7}$$

The traction $\boldsymbol{T}$ at a fault point $\boldsymbol{x}$ is defined as a continuous vector:

$$\boldsymbol{T}(\boldsymbol{x}, \boldsymbol{n}, t) = \boldsymbol{\sigma} \cdot \boldsymbol{n}, \tag{2.8}$$

$$[\boldsymbol{T}]^{\pm} = 0, \tag{2.9}$$

where $\boldsymbol{n}$ is a unit vector normal to the fault plane pointing from the "-" side to the "+". The main source of initial traction is tectonic loading and residual stress from previous seismic events.

Following Moczo et al. (2007), we first define the frictional strength and then state two conditions that constrain the traction. The frictional strength $S(\boldsymbol{x}, t)$ is defined as follows:

$$S = \mu_f(\boldsymbol{s}, \dot{\boldsymbol{s}}, \theta)|\boldsymbol{T_n}|, \tag{2.10}$$

where $\boldsymbol{T_n}$ denotes the normal component of traction on the fault, μ_f is a friction coefficient, and $\boldsymbol{\theta}$ denotes any additional state parameters. First condition states that the value of the shear traction on the fault T^{sh} (i.e., the tangential traction to the fault) is upper bounded by the frictional strength $S(\boldsymbol{x}, t)$:

$$T^{sh}(\boldsymbol{x}, t) \leq S(\boldsymbol{x}, t). \tag{2.11}$$

Second condition states that the shear traction behaves oppositely to the discontinuity in slip velocity, i.e., the slip velocity and traction are collinear, and the following holds:

$$\boldsymbol{T^{sh}}(\boldsymbol{x}, t)|\dot{\boldsymbol{s}}(\boldsymbol{x}, \boldsymbol{t})| - S(\boldsymbol{x}, t)\dot{\boldsymbol{s}}(\boldsymbol{x}, t) = 0. \tag{2.12}$$

In our case, the frictional boundary conditions on the fault are implemented using the traction at split node method. The fault is discretized by a split node surface mesh, which divides the space into two half-spaces ("+" and "-") that interact only at selected nodes on the fault. At each point on the grid, there are two partial nodes, each belonging to one side of the fault. These nodes share certain properties, such as slip, slip velocity, and friction coefficients, but differ in others, including mass, displacement vector, particle velocity, forces, and material parameters. If the material parameters on both sides of the fault are equal, the equations of the method simplify significantly, as the discontinuous components of velocity $\boldsymbol{v}$ and stress $\boldsymbol{\sigma}$ are antisymmetric, while the continuous components are symmetric. More details on this method and its implementation can be found in the appendix of Premus et al. (2020), which is based on Dalguer and Day (2007).

2.1.3 Friction law

The friction laws determine the processes in the cohesive zone, which is a zone behind the rupture front, where the value of friction decreases and the points (denoted + and -) start to slip. There are two empirical friction laws derived from small-scale laboratory experiments commonly used in dynamic modeling of earthquake rupture propagation: the rate-and-state and linear slip-weakening friction law. The former can be applied to coseismic, postseismic, and interseismic slip, whereas the latter can be applied only to coseismic slip.

According to the **rate-and-state** (R&S) friction law the strength S depends on the slip rates and the contact state variable Ψ:

$$S(\dot{s}, \Psi) = |\boldsymbol{T_n}|\mu_f(\dot{s}, \Psi), \tag{2.13}$$

$$\frac{d\Psi}{dt} = F(s, \dot{s}, \Psi), \tag{2.14}$$

where the behavior of Ψ in time is described by the so-called evolution law (Moczo et al., 2007).

In the literature, there are several types of this friction law. Here we present R&S friction law with **fast-velocity-weakening** following Premus et al. (2022), in the version by R. A. Harris et al. (2018):

$$S(\dot{s}, \Psi) = |\boldsymbol{T_n}|a\text{arcsinh}\left[\frac{\dot{s}}{2\dot{s_0}}\exp\left(\frac{\Psi}{a}\right)\right], \tag{2.15}$$

$$\frac{d\Psi}{dt} = -\frac{\dot{s}}{L}(\Psi - \Psi_{ss}), \tag{2.16}$$

$$\Psi_{ss} = a \log\left[\frac{2\dot{s_0}}{\dot{s}} \sinh\left(\frac{f_{ss}}{a}\right)\right], \tag{2.17}$$

$$f_{ss} = f_w + \frac{f_{LV} - f_W}{(1 + (\dot{s}/\dot{s_W})^8)^{1/8}}, \tag{2.18}$$

$$f_{LV} = f_0 - (b - a) \log\left(\frac{\dot{s}}{\dot{s_0}}\right), \tag{2.19}$$

where L is a characteristic slip, Ψ_{SS} denotes the steady-state value, f_{SS} denotes the steady-state friction, f_w is a fully weakened friction and f_{LV} is a low-velocity steady-state friction coefficient. The difference $(b - a)$ distinguishes the velocity-weakening $(b-a > 0)$ and velocity-strengthening $(b-a < 0)$ friction model regime.

The **linear slip-weakening** (SW) friction law states that the magnitude of the friction coefficient μ_f depends only on the cumulative magnitude of the slip s, and in the formulation of Ida (1972), and Andrews (1976) reads:

$$\mu_f = \begin{cases} \mu_s - (\mu_s - \mu_d)s/D_c, & \text{if } s < D_c \\ \mu_d, & \text{if } s \geq D_c \end{cases}$$

where μ_s (μ_d) is a static (dynamic) friction coefficient, and D_c denotes the so-called slip weakening distance. Equivalently, we can rewrite it using the shear (frictional) traction value T_f^{sh}:

$$T_f^{sh} = \begin{cases} T_s - (T_s - T_d)s/D_c, & \text{if } s < D_c \\ T_d, & \text{if } s \geq D_c \end{cases}$$

where the subscripts s and d denote the static and dynamic shear traction values, respectively. Alternatively, the linear SW friction law can be defined using the so-called slip path length (see Moczo et al. (2007)).

In other words, the magnitude of the shear traction (or the friction coefficient) depends only on the total slip distance. The force required to initialize the rupture is greater than the force required for further slipping. Slip occurs when the shear traction value reaches the static strength $T_s = S = \mu_s|\boldsymbol{T_n}|$ and then the stress decreases linearly with slip to the dynamic shear traction value $T_d = \mu_d|\boldsymbol{T_n}|$ on the interval of the slip-weakening distance D_c. After reaching the dynamic value, the shear stress is approximately constant with increasing slip. The difference between static strength and dynamic strength is commonly referred to as the strength drop, and the difference between strength and initial shear stress is the strength excess $T_s - T_i$. We define the prestress as a value above the dynamic shear traction $T_0 = T_i - T_d$.

The total energy involved in the rupture process is composed of radiated seismic energy, fracture energy, and heat energy. If $s_f > D_c$, we can define the fracture energy density contribution without heat G_f^{SW} and the radiated energy density E_R^{SW} in the following form:

$$G_F^{SW} = \frac{1}{2} D_c (T_s - T_d) \tag{2.20}$$

$$E_R^{SW} = \frac{1}{2} s_f (T_i - T_d) - \frac{1}{2} D_c (T_s - T_d), \tag{2.21}$$

T_f is a final value of the shear traction, and s_f denotes the final value of the slip; see Figure 2.1.

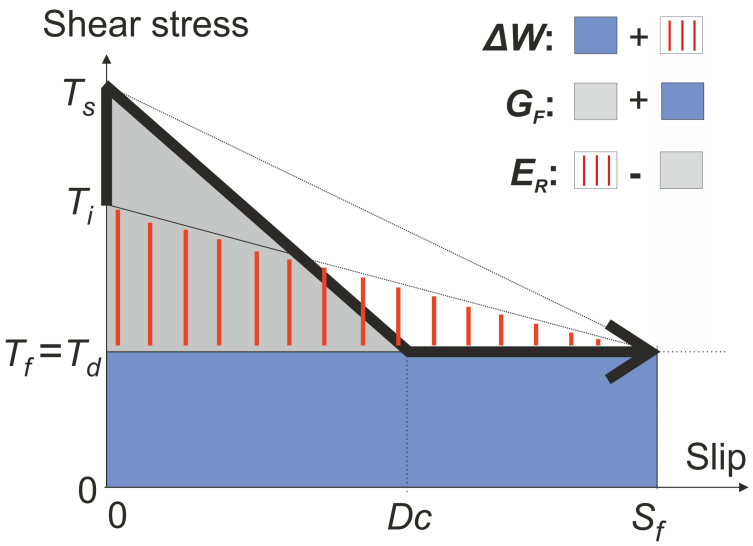


Figure 2.1 Linear slip-weakening law of friction as a function of shear traction on slip (thick black line). T_s denotes the value of the static strength, T_i the value of the initial shear traction, T_d the dynamic shear traction and T_f the final value of shear traction, D_c is the slip weakening distance and S_f the final value of slip. The gray plus blue area in the plot corresponds to the areal fracture energy density G_F, E_R is a density of radiated energy, and ΔW elastic energy. In the literature, fracture energy is usually considered without the heat energy contribution (blue area).

2.1.4 Outer boundary conditions

In seismology, it is common to prescribe the **free surface** condition at the top boundary between the atmosphere, here treated as a vacuum, and the solid ground. It is a reflective interface, where the zero-traction condition is assumed without restrictions on displacements (Stein and Wysession, 2003):

$$\boldsymbol{T} = \boldsymbol{\sigma} \cdot \boldsymbol{n} \Big|_{z=z_s} = 0, \tag{2.22}$$

where $\boldsymbol{n}$ is a normal vector to the free surface and z_s is a z coordinate of the free surface. If we assume $\boldsymbol{n}$ in the direction of the z-axis, we can write the equations on the surface:

$$T_i = \sigma_{i3} n_3 = 0 \implies \sigma_{13} = \sigma_{23} = \sigma_{33} = 0. \tag{2.23}$$

In the FD3D code (see Premus et al. (2020)), the free surface is numerically implemented using the stress imaging method, following Graves [1996].

The **absorbing boundary** is used for open interfaces where it is necessary to model free wave propagation without reflections. This is achieved by attenuating the elastic waves at the boundary. In the code, the absorbing conditions are implemented by the method of perfectly matched layers, which is explained in detail in the appendix of the Premus et al. (2020).

2.1.5 Overview of rupture parameters

This section contains the definitions of parameters characterizing earthquake rupture models, which can be categorized into two groups: kinematic and dynamic.

Kinematic parameters

The **rupture time** t_R is the moment when the rupture front reaches a given location on the fault.

The **rise time** t_{rise} denotes the time from t_R required for a fault point to reach its final slip s_f.

In this work, the **rupture area** A_R is defined as the area where the slip reaches at least 10 % of its maximum value.

The **rupture duration** is defined as the time interval required for this area to develop.

The **Rupture velocity** is defined as an inverse gradient of the rupture time $\boldsymbol{p}(\boldsymbol{x})$:

$$v_R = \frac{1}{\|\boldsymbol{p}(\boldsymbol{x})\|} = \frac{1}{\|\nabla t_R(\boldsymbol{x})\|}. \tag{2.24}$$

It is also common to use parameters averaged over the fault and slip-weighted. It is a spatially averaged quantity where each point on the fault contributes to the average in proportion to how much slip occurred there. For example, the slip-weighted average rupture velocity is defined as:

$$\overline{v_R} := \frac{\int_S \frac{1}{\|\boldsymbol{p}(\boldsymbol{x})\|}\|\boldsymbol{s_f}(\boldsymbol{x})\|\,dS}{\int_S \|\boldsymbol{s_f}(\boldsymbol{x})\|\,dS} = \frac{\sum_{i,j} \frac{1}{\|\boldsymbol{p}(i,j)\|}\|\boldsymbol{s_f}(i,j)\|}{\sum_{i,j} \|\boldsymbol{s_f}(i,j)\|}. \tag{2.25}$$

Moment rate function $\dot{M}_0(t)$, **seismic moment** M_0, and **moment magnitude** M_w are defined as (Aki and Richards, 2002):

$$\dot{M_0} = \int_A \mu(\boldsymbol{x})\|\dot{\boldsymbol{s_f}}(\boldsymbol{x},t)\|\,dA, \tag{2.26}$$

$$M_0 = \int_0^T \dot{M}_0(t)\,dt = \int_A \mu(\boldsymbol{x})\|\boldsymbol{s_f}(\boldsymbol{x})\|\,dA, \tag{2.27}$$

$$M_w = \frac{2}{3}(\log(M_0) - 9.1), \tag{2.28}$$

where $\boldsymbol{s_f}$ is the final slip, $\mu(\boldsymbol{x})$ is a shear modulus, A is the fault area and T is the duration of the rupture.

Dynamic parameters

The **stress drop** ΔT is the difference between the prestress T_i and the final shear traction T_f:

$$\Delta \boldsymbol{T} = \boldsymbol{T_i} - \boldsymbol{T_f}. \tag{2.29}$$

The strength drop is the difference between the strength and the final shear traction:

$$\Delta T^{SD} = T_s - |\boldsymbol{T_f}|. \tag{2.30}$$

The slip-weighted average stress drop is defined:

$$\overline{\Delta T} = \frac{\int_A \Delta \boldsymbol{T}(\boldsymbol{x}) \cdot \boldsymbol{s_f}(\boldsymbol{x})\, dA}{\int_A \|\boldsymbol{s_f}(\boldsymbol{x})\|\, dA}.$$

Radiated energy in the form of seismic waves reads (following Ripperger et al. (2007)):

$$E_R = -\frac{1}{2}\int_A \Delta \boldsymbol{T}(\boldsymbol{x}) \cdot \boldsymbol{s}_f(\boldsymbol{x})\, dA - \int_0^{t_f} dt \int_A (\boldsymbol{T}(t, \boldsymbol{x}) - \boldsymbol{T}_i(\boldsymbol{x})) \cdot \dot{\boldsymbol{s}}(t, \boldsymbol{x})\, dA, \tag{2.31}$$

where t_f is the duration of the rupture and A is the fault area.

Fracture energy is the energy that must be exceeded on the fault for the rupture to continue in propagation, and **fracture energy rate** is its area density (Kostka et al., 2021)

$$E_F = \int_A G_F\, dA, \tag{2.32}$$

$$G_F = \int_0^{s_f} (\boldsymbol{T}(s) - \boldsymbol{T}(s_f)) \cdot d\boldsymbol{s}. \tag{2.33}$$

Radiation efficiency reads:

$$\eta_{rad} = \frac{E_R}{E_R + E_F}. \tag{2.34}$$

Scaled energy is defined as the ratio between radiated energy and seismic moment:

$$\epsilon_R = \frac{E_R}{M_0}. \tag{2.35}$$

The non-dimensional ratio of dynamic stress drop to strength drop **stress level** (Ripperger et al., 2007) is as follows:

$$SL = \frac{T_i - T_d}{T_s - T_d}. \tag{2.36}$$

The strength excess ΔT^{SE} is defined as the difference between the fault strength and the initial shear traction:

$$\Delta T^{SE} = T_s - |\boldsymbol{T_i}|. \tag{2.37}$$

The **nucleation zone size** A_N is defined as an area where the initial shear traction T_i equals or exceeds the strength T_s, that is, where the strength excess value is negative or equal to zero ($\Delta T^{SE} <= 0$).

The **nucleation overstress** is the amount by which the initial shear traction T_i exceeds the strength T_s in the nucleation area.

The **rupture nucleation center** along strike and dip (x_0,y_0) is defined as a center of the nucleation zone.

2.2 Synthetic waveforms and static displacements

The elastodynamic Green function is defined as a solution of the elastodynamic equation for force excitation in the form of a Dirac delta function in space and time applied at the source position $\boldsymbol{\xi}$ at the origin time τ in the n direction. The i-th component of the elastic displacement at the receiver position $\boldsymbol{x}$ and time t is a Green tensor component $G_{in}(\boldsymbol{x}, t, \xi, \tau)$ and the following elastodynamic equation holds (Aki and Richards, 2002):

$$\rho \frac{\partial^2}{\partial t^2} G_{in} = \delta_{in}\, \delta(\mathbf{x} - \boldsymbol{\xi})\, \delta(t - \tau) + \frac{\partial}{\partial x_j} \left(c_{ijkl} \frac{\partial}{\partial x_l} G_{kn} \right). \tag{2.38}$$

From the space-time slip distribution on the fault, we can derive the elastic displacements everywhere using the representation theorem (Aki and Richards, 2002):

$$u_n(\mathbf{x}, t) = \iint_A s_i\, n_j c_{ijpq} * \frac{\partial}{\partial \xi_q} G_{np}\, dA, \tag{2.39}$$

where A is the fault area, s_i is a slip, n_j is a unit normal vector of the fault, c_{ijkl} is an elastic tensor and $*$ denotes the time convolution.

2.2.1 Synthetic waveforms

From dynamic simulation of the rupture propagation, we obtain the distribution of the slip rate function $\dot{\mathbf{s}}(\boldsymbol{\xi}, \tau)$ on the fault. If we divide the fault into M subfaults with areas A_m, due to the additivity of the integral, the representation theorem can be rewritten as a sum over individual subsources.

$$u_n(\mathbf{x}, t) = \sum_{m=1}^{M} \iint_{A_m} s_i\, n_j c_{ijpq} * \frac{\partial}{\partial \xi_q} G_{np}\, dA_m. \tag{2.40}$$

Now we differentiate the equation and express the slip rates in the form of their magnitude and unit direction vector $\dot{s}_i = \dot{s}\nu_i$, and further assume a time-independent rake, introduce a modified Green's tensor H, and use the convolution commutative property:

$$\begin{aligned} \dot{u_n}(\mathbf{x}, t) &= \sum_{m=1}^{M} \iint_{A_m} \dot{s}\nu_i\, n_j c_{ijpq} * \frac{\partial}{\partial \xi_q} G_{np}\, dA_m \\ &= \sum_{m=1}^{M} \iint_{A_m} \nu_i\, n_j c_{ijpq} \frac{\partial}{\partial \xi_q} G_{np} * \dot{s}\, dA_m \\ &= \sum_{m=1}^{M} \iint_{A_m} H_n * \dot{s}\, dA_m. \end{aligned} \tag{2.41}$$

There are many methods to numerically calculate the Green's tensor. We use the AXITRA code (Cotton and Coutant, 1997), which is based on the discrete wavenumber method for a 1D layered medium. In a 3D medium, some numerical methods, such as finite element (e.g., SPECFEM3D by Komatitsch et al. (2023)),

finite difference (e.g., SW4 by Petersson et al. (2023)), or spectral element (e.g., IRIS SYNGINE by Hutko et al. (2017)) method, are needed.

We now apply the mean value theorem. By spatial averaging (see Figure 3.3), we can determine the mean value of the slip rate on the m-th subfault $\overline{\dot{s}_m(\tau)}$. If the discretization of the fault into subfaults is sufficient, and using the properties of our precomputed modified Green functions $H_n(\boldsymbol{x}, t, \boldsymbol{\xi})$ for each station-subfault combination, we can derive the following:

$$\begin{aligned} u_n(\boldsymbol{x}, t) &= \sum_{m=1}^{M} H_n(\boldsymbol{x}, t, \boldsymbol{\xi_m}) * \int_{A_m} \dot{s}(\boldsymbol{\xi}, t)\, dA_m \\ &= \sum_{m=1}^{M} H_n(\boldsymbol{x}, t, \boldsymbol{\xi_m}) * \left(\overline{\dot{s}_m(t)}\, A_m\right) = A_m \sum_{m=1}^{M} H_n(\boldsymbol{x}, t, \boldsymbol{\xi_m}) * \overline{\dot{s}_m(t)}. \end{aligned} \quad (2.42)$$

The waveform at each station located at position ($\boldsymbol{x}$,t) is thus computed by summing, over all subfaults, the convolution of the precomputed Green's functions with the corresponding subfault-average slip rates; each is weighted by the respective subfault area A_m. In our case, A_m is constant due to the uniform, regular fault discretization.

2.2.2 Static displacements

Okada (1985) derived analytical formulas for static displacement for a homogeneous rectangular source with constant slip. We use the following formula for the static displacement component u_n of an inhomogeneous fault composed of M individual subfaults:

$$u_n(\boldsymbol{x}) = \sum_{m=1}^{M} s_f^m\, G_n(m, \boldsymbol{x}), \quad (2.43)$$

where the subscripts n represent the north, east and vertical components, respectively, s_f^m is the total slip in the subfault m and G_n is a static Green's functions ($t \to \infty$) for each component calculated for every combination of subfault m and each GNSS station located at $\boldsymbol{x}$. The static Green's functions are calculated following Okada (1985). Here, the slip value for each subfault s_f^m is obtained by integrating the averaged slip rates:

$$s_f^m = \int_0^T \overline{\dot{s}_m(t)}\, dt, \quad (2.44)$$

2.3 Inverse problem

2.3.1 Formulation of the inverse problem

In a Bayesian formulation, the results of the inverse problem are given by the posterior probability density function (posterior PDF), also known as the a posteriori PDF, which contains information from both the data and data-independent prior information and reads:

$$p(\boldsymbol{m}|\boldsymbol{d}) = \frac{p(\boldsymbol{m})p(\boldsymbol{d}|\boldsymbol{m})}{p(\boldsymbol{d})}, \tag{2.45}$$

where $p(\boldsymbol{d})$ is the so-called Bayesian evidence here serving as a normalization constant; prior (or a priori) model PDF $p(\boldsymbol{m})$ contains information on the constraints of the model parameters; and $p(\boldsymbol{d}|\boldsymbol{m})$ is the so-called likelihood function, i.e. the PDF of the data $\boldsymbol{d}$ given a model $\boldsymbol{m}$ (Sambridge, 2013; Tarantola, 2005).

We assume that the likelihood function $L(\boldsymbol{m})$ is Gaussian with diagonal covariance function:

$$L(\boldsymbol{d}, \boldsymbol{m}) = p(\boldsymbol{d}|\boldsymbol{m}) = c_1 \exp\left\{-\frac{1}{2}\sum_{i=1}^{N}\frac{\|\boldsymbol{s_i}(\boldsymbol{m}) - \boldsymbol{d_i}\|^2}{\sigma_i^2} - \frac{1}{2}\frac{(M_w(\boldsymbol{m}) - M_w^0)^2}{\sigma_{M_W}^2}\right\}, \tag{2.46}$$

where $\boldsymbol{d_i}$ and $\boldsymbol{s_i}(\boldsymbol{m})$ are observed and synthetic data at station i, N is the number of stations, σ_i is an assumed standard deviation of displacements at a given station that represents the combined uncertainty of both the modeling and the data errors, $M_w(\boldsymbol{m})$ means the moment magnitude for the model parameters $\boldsymbol{m}$, M_w^0 is the prescribed moment magnitude with its standard deviation σ_{M_W}. Here we define a misfit as a sum over all stations and components of the L2 norm of the difference between the observed $\boldsymbol{d}$ and synthetic $\boldsymbol{s}(\boldsymbol{m})$ data weighted by the corresponding sigma standard uncertainty.

The model prior PDF $p(\boldsymbol{m})$ is assumed to be uniform with zero values outside the specified interval:

$$p(\mathbf{m}) \propto \begin{cases} k, & \text{if } (m_{\min}^{prior})_i \leq m_i \leq (m_{\max}^{prior})_i, \\ 0, & \text{otherwise,} \end{cases}$$

where k is a real normalization constant.

Let us denote an indicator $I_N(\boldsymbol{m})$. The indicator function multiplies the posterior PDF, and it verifies whether the nucleation satisfies the given condition:

$$I_N(\boldsymbol{m}) \propto \begin{cases} 1, & \text{if the conditions on the nucleation are satisfied,} \\ 0, & \text{otherwise.} \end{cases}$$

Combining all components, the posterior probability density function (PDF) is expressed as follows:

$$\begin{aligned} p(\boldsymbol{m}|\boldsymbol{d}) &= Cp(\boldsymbol{m})I_N(\boldsymbol{m}) \\ &\times \exp\left(-\frac{1}{2}\sum_{i=1}^{N}\frac{\|\boldsymbol{s_i}(\boldsymbol{m}) - \boldsymbol{d_i}\|_2^2}{\sigma_i^2} - \frac{1}{2}\frac{(M_w(\boldsymbol{m}) - M_w^0)^2}{\sigma_{M_W}^2}\right), \end{aligned} \tag{2.47}$$

where C is a normalization constant.

Since our model parameter vector space is high-dimensional, a systematic exploration of the model space is impossible. Moreover, we do not know the normalization constants, so we cannot evaluate the posterior PDF appropriately. It is why we use the Metropolis-Hastings (MH) Markov Chain Monte Carlo (MCMC) algorithm to sample the posterior distribution of the model parameters. The method is based on the ratio between the posterior PDF values of two models $\boldsymbol{m_i}$ and $\boldsymbol{m_j}$, so we do not need to evaluate the normalization constant. MCMC performs a random walk through the model space. According to the Markov property, the probability of visiting the next point in the model space depends only on the current point in the model space and not on the previous ones. A new sample m_j is accepted with probability $P(\boldsymbol{m_i} \rightarrow \boldsymbol{m_j})$, otherwise, the Markov chain remains at $\boldsymbol{m_i}$. The probability of the transition from the model point $\boldsymbol{m_i}$ to $\boldsymbol{m_j}$ is given by the Metropolis-Hastings acceptance rule (Sambridge and Mosegaard, 2002):

$$P(\boldsymbol{m_i} \rightarrow \boldsymbol{m_j}) = \min\left(1, \frac{p(\boldsymbol{m_j}|\boldsymbol{d})q(\boldsymbol{m_i}|\boldsymbol{m_j})}{p(\boldsymbol{m_i}|\boldsymbol{d})q(\boldsymbol{m_j}|\boldsymbol{m_i})}\right),$$

where $p(\boldsymbol{m_j}|\boldsymbol{d})$, resp. $p(\boldsymbol{m_i}|\boldsymbol{d})$, is a posterior PDF in the model $\boldsymbol{m_j}$, $\boldsymbol{m_i}$ respectively, and $q(\boldsymbol{m_j}|\boldsymbol{m_i})$ is a proposal distribution, suggesting a new state $\boldsymbol{m_j}$ given the current state $\boldsymbol{m_i}$. Note that in the case of the normal distribution (or any other symmetric distribution) $\frac{q(\boldsymbol{m_i}|\boldsymbol{m_j})}{q(\boldsymbol{m_j}|\boldsymbol{m_i})} = 1$. In this work, we assume a log-normal proposal distribution:

$$m_j^{(k)} = m_i^{(k)} \cdot exp(\epsilon_k \Delta m^{(k)}), \tag{2.48}$$

where $\epsilon_k \sim \mathcal{N}(0,1)$ is a random number drawn from a standard normal distribution and Δm is a stepsize for the k-th component of the model space vector with dimension N. In that case, the following holds:

$$\frac{q(\mathbf{m}_i|\mathbf{m}_j)}{q(\mathbf{m}_j|\mathbf{m}_i)} = \prod_{k=1}^{N} \frac{m_j^{(k)}}{m_i^{(k)}}. \tag{2.49}$$

To improve the efficiency of probabilistic sampling and better convergence, we use the Parallel Tempering MCMC method with modified MH rule (Sambridge, 2013). Here, the model space is explored using multiple MCMC chains at different temperature levels T. The likelihood function is modified by the temperature parameter T and reads with a normalization constant k_T following Sambridge and Mosegaard (2002) as follows:

$$p(\boldsymbol{d}|\boldsymbol{m_i}) \rightarrow p(\boldsymbol{d}|\boldsymbol{m_i}, T) = k_T p(\boldsymbol{d}|\boldsymbol{m_i})^{1/T},$$

and the posterior probability density function (PDF) is expressed as follows:

$$\begin{aligned} p(\boldsymbol{m}|\boldsymbol{d}, T) = {} & C p(\boldsymbol{m}) I_N(\boldsymbol{m}) \\ & \times \exp\left(-\frac{1}{2T}\sum_{i=1}^{N} \frac{\|\boldsymbol{s_i}(\boldsymbol{m}) - \boldsymbol{d_i}\|_2^2}{\boldsymbol{\sigma_i^2}} - \frac{1}{2T}\frac{\left(M_w(\boldsymbol{m}) - M_w^0\right)^2}{\sigma_{M_W}^2}\right), \end{aligned} \tag{2.50}$$

where C is a normalization constant.

The target distribution is sampled by chains at $T = 1$. At low temperatures, the chains perform localized exploration in the vicinity of a local maximum, whereas higher temperatures can help to escape from the local minima and better move through the multimodal density model space.

Each chain i and j, with neighboring temperature levels T_i and T_j, can exchange the vectors of the model parameters $\boldsymbol{m_i}$ and $\boldsymbol{m_j}$:

$$(\boldsymbol{m_i}, T_i), (\boldsymbol{m_j}, T_j) \rightarrow (\boldsymbol{m_i}, T_j), (\boldsymbol{m_j}, T_i).$$

The probability of the swap $\alpha(i, j)$ can be expressed in an MH form that is again independent of the normalization constant:

$$\alpha(i,j) = \min\left(1, \left[\frac{p(\boldsymbol{d}|\boldsymbol{m_j}, T_j)}{p(\boldsymbol{d}|\boldsymbol{m_i}, T_i)}\right]^{\frac{1}{T_i}} \left[\frac{p(\boldsymbol{d}|\boldsymbol{m_i}, T_i)}{p(\boldsymbol{d}|\boldsymbol{m_j}, T_j)}\right]^{\frac{1}{T_j}}\right). \tag{2.51}$$

We have already defined the misfit as an L2 norm between the observed and synthetic data in Equation (2.46). To quantify the fit between observed data $\boldsymbol{d}$ and synthetics $\boldsymbol{s}(\boldsymbol{m})$, it is also common to use variance reduction:

$$VR = 1 - \frac{||\boldsymbol{s}(\boldsymbol{m}) - \boldsymbol{d}||^2}{||\boldsymbol{d}||^2}. \tag{2.52}$$

Note that if we obtain a large collection of samples from the posterior PDF, we can approximate the samples of the 1D marginal PDF for some model parameter m_k simply by collecting its values from the samples of the posterior PDF. The mean value is then given simply by the arithmetic mean.

Let the samples be $x_1, x_2, \ldots, x_N$. Then the mean and the biased (aka population) standard deviation are given by (Wackerly et al., 2008):

$$\bar{x} = \frac{1}{N}\sum_{i=1}^{N} x_i$$
$$\sigma_{\text{biased}} = \sqrt{\frac{1}{N}\sum_{i=1}^{N} x_i^2 - (\bar{x})^2}.$$

The Pearson product-moment correlation coefficient ρ measures the linear relationship between two variables x_i and y_i. The equation is as follows:

$$\rho(x_i, y_i) = \frac{\sum_{i=1}^{n}(x_i - \bar{x})(y_i - \bar{y})}{\sqrt{\sum_{i=1}^{n}(x_i - \bar{x})^2}\sqrt{\sum_{i=1}^{n}(y_i - \bar{y})^2}}. \tag{2.53}$$

2.3.2 Algorithm of the inverse problem

First, we need to define the model parameters (prestress T_0, friction drop $\mu_s - \mu_d$, and slip-weakening distance D_c) and their prior constraints, as well as the nucleation constraints I_N. Next, we need to specify MCMC settings, including the proposal distribution and step sizes. Finally, before running the inversion, we need to define the initial model. In the following, we provide a brief overview of the main steps of the algorithm for our inverse problem.

1. Modification of the model parameters following the lognormal proposal distribution.

2. Verification of whether the model parameters satisfy the prior bounds. If not, it returns to Step 1. It corresponds to multiplication by $p(\boldsymbol{m})$ in the posterior PDF equation (Equation (2.50)).

3. Calculation of the nucleation zone and the mean nucleation overstress. Verification of whether nucleation occurs within the specified region with the prescribed radius around the hypocenter, and if the mean nucleation overstress is less than 1 MPa. If not, back to step 1. It corresponds to the multiplication by $I_N(\boldsymbol{m})$ in Equation (2.50).

4. Dynamic rupture simulation.

5. Calculation of synthetic seismic waveforms and static displacements, and evaluation of the misfit.

6. Decision whether the model is accepted or not, following the Metropolis-Hastings acceptance rule (Equation (2.3.1)). If not, the algorithm goes back to Step 1.

7. Exchanging model samples between chains with neighboring temperatures with the probability $\alpha(i, j)$ according to the Equation (2.51).

8. The accepted model is the current model, and the algorithm goes back to Step 1.

3 Data and method

3.1 Data, velocity model and aftershocks

We use three-component strong motion data from 21 seismic stations located within an epicentral distance of 50 km recorded by the K-NET (Kyoshin Network) and KiK-net (Kiban Kyoshin Network) seismograph network operated by NIED (Earth Science and Resilience, 2019), downloaded from (`https://www.kyoshin.bosai.go.jp/`); see Figure 3.1. We applied a fourth-order causal Butterworth filter utilizing XAPiir, a recursive digital filtering package by D. Harris (1990). The data are numerically integrated into velocities and bandpass filtered between 0.05 and 1.0 Hz for the nearest station located 6 km from the epicenter (Kurayoshi, TTR005), from 0.1 to 0.6 Hz for the second nearest station in the epicentral distance 10 km (Sekigane, TTRH07) and from 0.05 to 0.5 Hz for others. The high-pass filter is applied in order to remove noise from the data, especially instrumental noise, while the low-pass filter is used to minimize the impact of the imperfect velocity model in calculating the synthetic Green's functions, imprecise location, fault geometry, and unknown crustal heterogeneities.

We use horizontal and vertical coseismic static displacements from 13 GNSS Earth Observation Network stations deployed by the Disaster Prevention Research Institute (DPRI) of Kyoto University, inferred by Meneses-Gutierrez et al. (2019), and 25 GNSS stations operated by the Geospatial Information Authority of Japan (GSI), inferred by Amey et al. (2019).

We consider the uncertainties of seismic and geodetic data as a setup parameter of the inverse problem; therefore, it can be found below in 3.2.3.

The 1D Crustal model was extracted from the 3D Japan Integrated Velocity Structure Model (Koketsu et al., 2008; Koketsu, Miyake, et al., 2012). To mitigate site effects, we extracted the crustal model under each seismic station individually; see Figure 3.2.

The locations of the aftershocks and foreshocks are adopted from Ross et al. (2018), who used the template matching algorithm to detect previously unidentified earthquakes in the continuous data.

3.2 Methods

We used the fd3d_tsn_pt code (Gallovič et al., 2019a) for dynamic rupture propagation simulation, calculation of synthetic seismograms and static displacements, and dynamic inversion. The method was introduced and validated on a community slip-inversion benchmark test by Mai et al. (2016) for coseismic data with a slip-weakening friction law in Gallovič et al. (2019a). It was applied to the 2016 Mw 6.2 Amatrice earthquake (Gallovič et al., 2019b), to the 2020 Mw 6.8 Elazığ earthquake (Gallovič et al., 2020), used to generate and analyze a synthetic event database to supplement the data for GMM in Gallovič and Valentová (2020), and applied to the 2017 Mw 6.3 Lesvos earthquake in Kostka et al. (2021). Lately, the code was supplemented by the fast-velocity-weakening rate-and-state friction law with coseismic and postseismic slip and applied to the Mw 6.0 2014 South

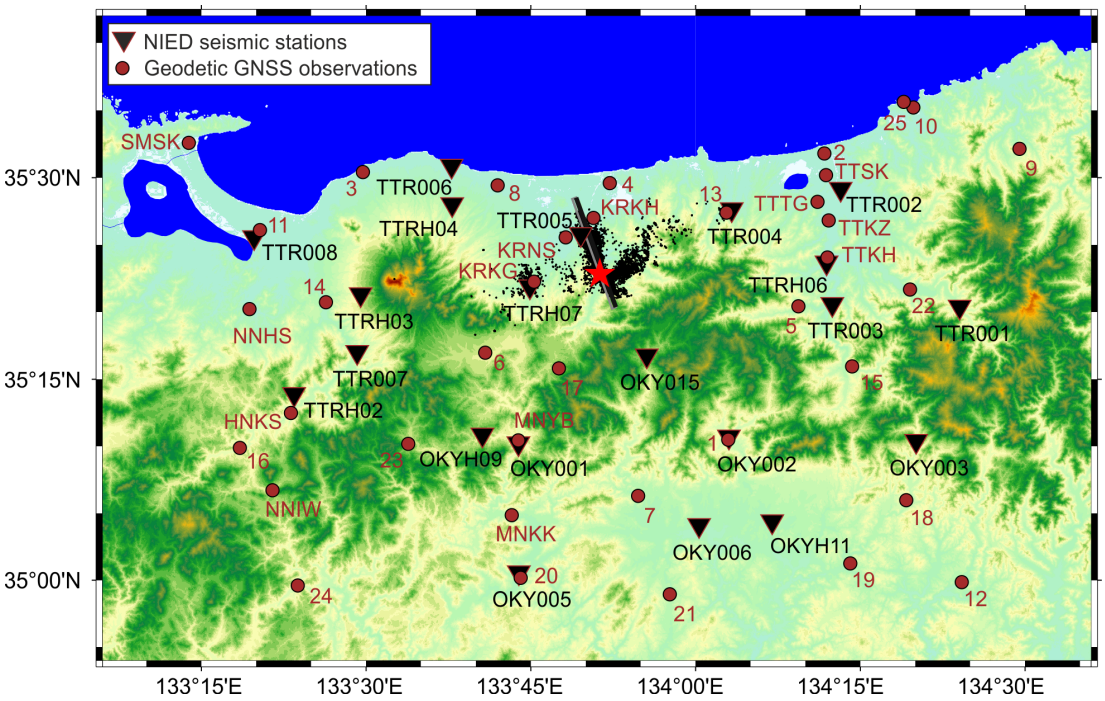


Figure 3.1 Map of NIED seismic stations (triangles) and geodetic GNSS observations (circles, DPRI marked with their name and GSI marked with numbers) used in this work. The black and gray lines represent the surface projections of the upper and lower along-strike sections of the fault, respectively. The red star indicates the location of the hypocenter, whereas the black dots denote the positions of foreshocks and aftershocks.

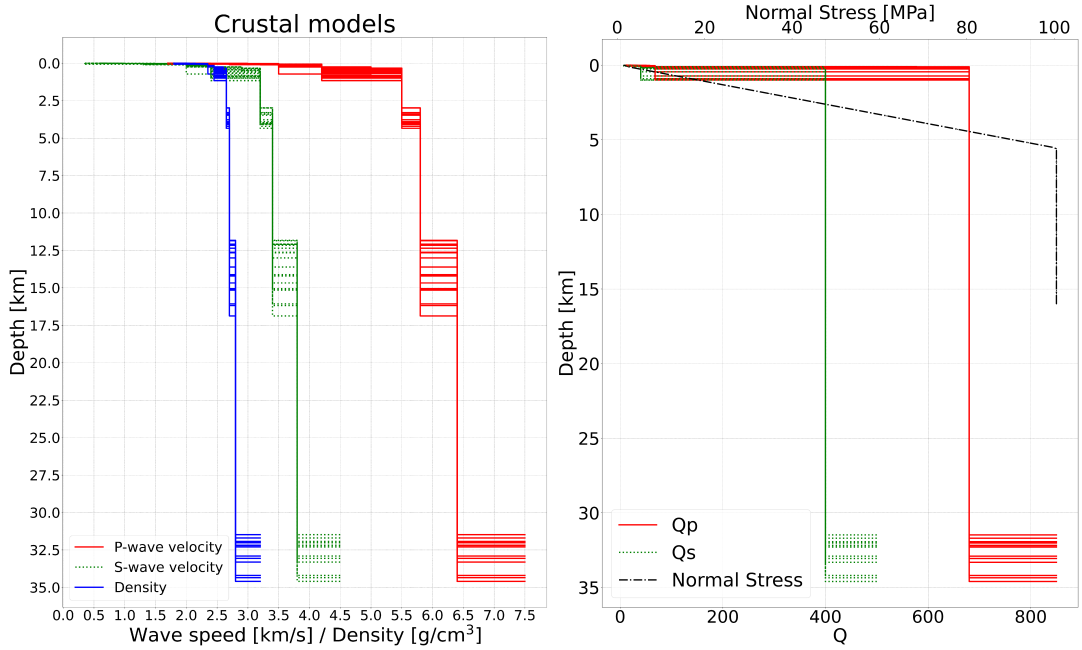


Figure 3.2 Crustal models used for calculating Green's functions on the left and an anelastic attenuation factor with depths on the right. Parameters are extrapolated from the Japan Integrated Velocity Structure Model (Koketsu, Miyake, et al., 2012) for each station separately. Normal stress was set to increase linearly in the shallower regions to 100 MPa at 5.6 km depth and constant below.

Parameter	Value
General	
Fault dimension	Length 16 km, width 16 km
Fault top depth	0 km
Fault mechanism	Strike 160°, dip 88°, rake 0°
Hypocenter location	35.3806° N, 133.8545° E, depth 11.58 km
FD3D	
Spatial discretization	100 m
FD half-domain size (along strike, normal, dip)	161, 110, 161
Number of time step (FD)	5 000
Time step in seconds (FD)	2 ms
Dip	90°
Computational time (GPU)	15 s
Green's functions	
Spatial fault discretization	1 km
Maximum computed frequency	2.5 Hz (Nyquist)
Time sampling	0.2 s
Inversion parameters	
Number of model parameters (discretization)	11, 11
Prestress prior	(0;100) MPa
Static-Dynamic friction coefficient prior	(0; 1.0)
Characteristic slip-weakening distance prior	(0.04; 2.0) m
Nucleation position (along strike, up dip)	11 km, 4.5 km
Nucleation radius prior	1000 m
Data and modeling errors	
Seismic data uncertainty	0.05 m
Mw uncertainty	(6.05; 6.25)

Table 3.1 Parameters for forward FD simulation, Green's functions, and dynamic inversion model setup.

Napa, California earthquake in Premus et al. (2022) and to the Mw 6.0 2004 Parkfield earthquake in Schliwa et al. (2024). It was also used to conduct a simple parametric study applied to the 2016 Mw 6.2 Tottori earthquake in Hronek (2023). Here, we briefly introduce the method; for a more detailed theoretical background, see Chapter 2.

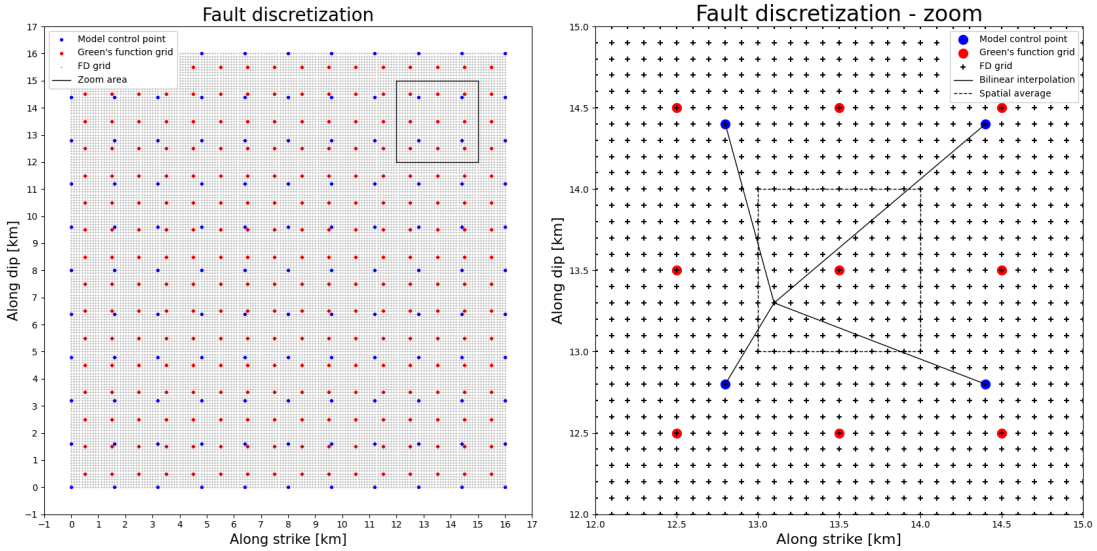


Figure 3.3 Fault discretization with three grids used in this work on the left, and zoom on the right; see Table 3.1. The first grid (blue circles) is the model control points, which contain model parameters: prestress, friction drop, and slip weakening distance. Model parameters are bilinearly interpolated (continuous black lines) on the densest FD grid used for dynamic rupture simulation. Calculated slip rates are then spatially averaged (the dashed square) onto a coarser grid that stores the precalculated Green's functions (red circles). Each averaged slip rates are then convolved with the corresponding Green's function in every GF grid point and summed up following the representation theorem for each station separately, thus obtaining the waveforms.

3.2.1 Forward problem

FD3D_TSN is an open-source Fortran code developed by Premus et al. (2020). Thanks to the simple geometry and GPU acceleration employed using the OpenACC programming model, it is quite fast compared to other codes. The code was verified and validated by Premus et al. (2020) using benchmark tests by the Southern California Earthquake Center-US Geological Survey (SCEC-USGS) dynamic rupture code validation group (R. A. Harris et al., 2018).

We assume a shear rupture on a frictional vertical planar fault that is orthogonal to the planar free surface. The elastodynamic equation is assumed in a classical velocity-stress formulation in isotropic material (Moczo et al., 2007) and is solved using the fourth-order FD method on a 3D staggered regular Cartesian grid (Graves, 1996; Madariaga et al., 1998). The fault frictional boundary condition is implemented by the traction at split node method following Dalguer and Day (2007). The free surface at the upper interface is modeled using the stress imaging method of Graves (1996). Absorbing boundary conditions at the remaining interfaces are implemented using perfectly matched layers in a split formulation following Kristek et al. (2009).

Two friction laws are implemented in the code: the first is the classical linear slip-dependent friction law (Andrews, 1976), and the second is the fast-velocity-weakening rate-and-state friction law, version used by R. A. Harris et al. (2018). In this work, we used the first one, the linear slip-weakening friction law.

The result of the dynamic simulation is a spatio-temporal distribution of slip

rates and tractions along the fault. Synthetic seismograms are then calculated by convolution of slip rates with Green's function precalculated using the Axitra code (Cotton and Coutant, 1997) and summed following the representation theorem (Aki and Richards, 2002). We apply the same filter to the synthetic seismograms as to the data. Static displacements are calculated following Okada (1985).

In rupture simulation, we consider a vertical fault with a dip of 90°, while for the calculation of the GF, we take into account the actual dip of 88°. The validity of this approach was tested on the 2016 Amatrice earthquake with a dip of 45° in Gallovič et al. (2019b).

The fault dimension is 16 km in both length and width with a spatial discretization of 100 m for the rupture simulation (finite difference grid) and 1 km for GF. Temporal discretization is 2 ms for FD and 200 ms for GF (see Table 3.1 and Figure 3.3). With this differentiation, the computational time on the Nvidia RTX 3070 GPU is only 15 s for one rupture simulation and waveform calculation.

3.2.2 Model parametrization and frictional law

We use the classical linear slip-weakening friction law as described in Chapter 2.1.3. For the forward problem, we need to prescribe the spatially inhomogeneous distribution of the prestress ($T_0 = T_i - T_d$) and the frictional parameters of the linear slip-dependent friction law (Figure 2.1), that is, the difference between the static and dynamic friction coefficient (friction drop, $\mu_s - \mu_d$) and the slip-weakening distance D_c.

The dynamic friction coefficient was set at a constant value of 0.4, as we consider that the absolute level of shear stress and strength has a negligible effect on the rupture propagation. The normal stress profile is shown in Figure 3.2. We added cohesion 0.5 MPa to the frictional strength to regularize the normal stress decrease to zero on the free surface.

3.2.3 Inverse problem

We formulate the inverse problem in a Bayesian framework with sampling of the posterior probability density function using the Monte Carlo Parallel Tempering Markov Chains algorithm (Sambridge and Mosegaard, 2002; Sambridge, 2013) with modified Metropolis-Hastings acceptance rule (Metropolis et al., 1953). For theoretical background see Chapter 2.3. We explore the model space using six MPI processes, each running eight parallel Markov chains at different temperatures; two of these eight chains have a temperature of $T = 1$ and sample the posterior PDF. Varied temperatures enable a more efficient search through the model space and prevent entrapment at a local minimum.

For the inverse problem, the fault is discretized by a grid of $11 \times 11 = 121$ model control points that contain three model parameters: prestress (T_0), friction drop ($\mu_s - \mu_d$), and slip-weakening distance (D_c). We assume uniform prior PDFs of these three model parameters within the wide ranges specified in Table 3.1. Note that these ranges of parameters are relatively wide to avoid overly constraining the model space search. We assume a log-normal proposal distribution for the model

parameters. We tested different proposal step sizes and achieved satisfactory convergence and model space sampling with step sizes of 4 % for T_o and $\mu_s - \mu_d$, and 2 % for D_c.

We set constraints on the seismic moment, although our joint inversion using both seismic and geodetic data probably does not necessarily require this. The prior seismic moment value is 2.1×10^{18} Nm, and the standard deviation ($\sigma_{M_W} = 0.1$) was prescribed to account for variations in results from different agencies and published articles.

We have prior information about the nucleation position from Ross et al. (2018) and Kubo et al. (2017), and we constrain the nucleation area with a prescribed diameter around the hypocenter. Firstly, we tested a low-constraint nucleation with a diameter of 2,500 m. This results in a group of reasonably good models with nucleation shallower than in the aforementioned researches, but with a relatively large time shift for seismic VR. Next, we reduced the allowed time shift for calculating seismic VR from 2 to 0.5 seconds and decreased the nucleation diameter from 2,500 to 1,000 meters, which improved the fit.

We consider the seismic data error standard deviation to be equal to 5 cm and tested different weights for the first two stations, as their amplitudes are significantly larger compared to others, but this did not lead to any improvement. Overall, the seismic stations are implicitly weighted only by their own recorded amplitude. We adopted the geodetic observation uncertainties from the respective articles and tested various weights to explore their resolution power. Overall, the GNSS uncertainties are multiplied by a factor of 8 to achieve a similar seismic and geodetic misfit in the later part of the initial burn-in phase, and individual records from various GNSS stations are implicitly weighted only by their own recorded amplitudes.

We tested multiple initial models. Considering the principles of the MCMC MH random walk method, a suitable initial model appears to be one with a large rupture area that covers the majority of the fault without reaching the edges, since it allows the algorithm to have the greatest variability in rupture behavior and in the MCMC exploration of the model space; see Figure 3.4. We used the same initial model for all chains. The fit of the initial model is relatively poor (seismic VR -0.61 and geodetic VR -3.18), but with a suitable parameter configuration, we managed to obtain a fairly fast convergence rate.

We conducted preliminary tests using slip-strengthening (SS) friction in the linear slip-dependent friction law as a replacement for velocity-strengthening in the rate-and-state framework. Considering the higher nucleation area prior (2500 m) and the greater time shift for seismic VR (2 s), we compared models with the linear slip-weakening (SW) friction alone and linear SS friction combined with SW. At shallow depths up to 4 km (or 2 km) we tried to prescribe the SS friction and otherwise the SW friction. This is because some kinematic inversion results suggest the possibility of shallow slip, but following the rheological models, we know that an earthquake cannot nucleate in the velocity-strengthening region. We concluded that SS is not a necessary feature for this event, because it did not lead to any improvement in the data misfit.

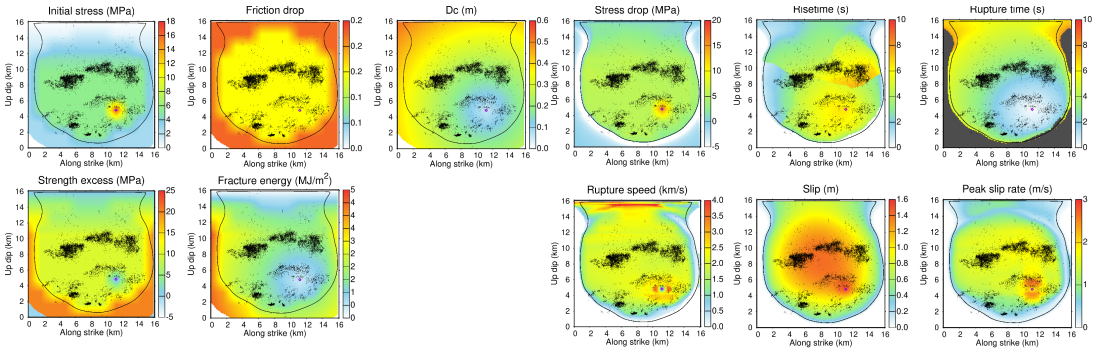


Figure 3.4 Initial model parameters on the fault. Black lines contour the slip, purple lines bound the nucleation, and black dots denote foreshocks and aftershocks projected on the fault plane. For parameter description, see Figs. 4.1 and 4.2.

For a complete list of the parameters of this study, see Table 3.1. In this configuration, after optimizing the parameters, we run the inversion without manually intervening in the process. We used parallel computing with 7 MPI processes on three Nvidia RTX 3070 GPUs. Each forward simulation takes about 15 s.

4 Results

The Markov chains explored approximately 1.2 million models in 82 days. Only one out of every ten samples was saved, and only samples at temperature $T = 0$ were saved since only temperature one samples the posterior PDF. We removed the first 40 % of the samples (extended burn-in phase). We also removed duplicate models with very similar properties. This results in a final set of 14,764 accepted models (the ensemble), which we use for further analysis.

In this chapter, we first introduce the maximum a posteriori (MAP) model as the best-fitting model with the lowest misfit. Next, we discuss the averaged properties of the inferred ensemble models, i.e., the result of the inverse problem in the Bayesian sense. Here we have not one result, but rather a family of results that can be described using means with standard deviations, histograms, heat maps, and a video of the parameters on the fault from randomly selected models from the ensemble.

4.1 Maximum a posteriori model

Table 4.1 provides the values of the MAP model rupture parameters. The distribution of the input and output parameters on the fault can be found in Figures 4.1 and 4.2, respectively. In Figure 4.3 we present the slip rate distribution on the subfaults, and in Figure 4.4, the temporal evolution of the horizontal component of the slip rate on the fault is shown. Figures 4.5 and 4.6 show the comparison between observed and synthetic GNSS horizontal components of static displacements and seismic waveforms, respectively.

We see that the fit of the observed GNSS static displacements is very good, with a variance reduction of 98.94%. Additionally, a reasonably good fit was achieved with the strong-motion seismographs, with a variance reduction of 54.99% for a time shift of 0.2 seconds. Improvements at the near stations are visible (see, e.g., stations TTR005, TTRH07, and OKY015), although some features remain unexplained. These features likely reflect the influence of the crustal model and local effects. The stations TTRH04 and TTR006 are located near the sea, which suggests the possible presence of sediments. The latter parts, which are probably caused by the coda, also remain unexplained.

The MAP model represents one of the possible rupture evolution scenarios. The rupture area is 93 km^2 with a maximum slip of approximately 2.1 m at a depth of approximately 5.5 km, located approximately 11.5 km along the strike. Most of the slip is confined to the region between the depths of 4 km and 12 km. The rupture first propagates more or less vertically upward (0-2.5 s), then splits into two parts with smaller slip values, one branch continues vertically and then along the strike direction up to approximately 1 km depth (up to 4 s), and the other branch extends along the strike direction (2.5-4.0 s), gently turning again toward the dip direction near the end (4.5-5 s).

The average (slip-weighted) stress drop across the fault is 7.75 MPa and the average (slip-weighted) rupture velocity is 2.06 km/s; however, we can see that the distribution on the fault is inhomogeneous with large value ranges. For instance,

in the vertical upward direction of the rupture propagation, the rupture speed values are above 3 km/s and the maximum stress drop is 30 MPa. The risetime is quite high near the nucleation point (about 9 s) and decreases with increasing distance.

The input dynamic parameter distributions on the fault are highly inhomogeneous. The maximum value of fracture energy density for plotting is set to 20 MPa, but the actual maximum value (outside of the rupture area) is much higher, approximately 40 MPa.

Parameter	Value
Rupture area A_R	92.76 km^2
Average speed $\overline{v_R}$	2 059 m/s
Seismic moment M_0	2.34×10^{18} Nm
Average stress drop $\overline{\Delta T}$	7.75 MPa
Fracture energy E_F	2.55×10^{14} J
Radiated energy E_R	4.01×10^{13} J
Radiation efficiency η_{rad}	13.6 %
Seismic misfit	43.69
Seismic VR	54.99 % for shift 0.2 s
GPS misfit	2.31
GPS VR	98.94 %

Table 4.1 Kinematic and dynamic parameters of the MAP model inferred by the Bayesian dynamic finite fault inversion.

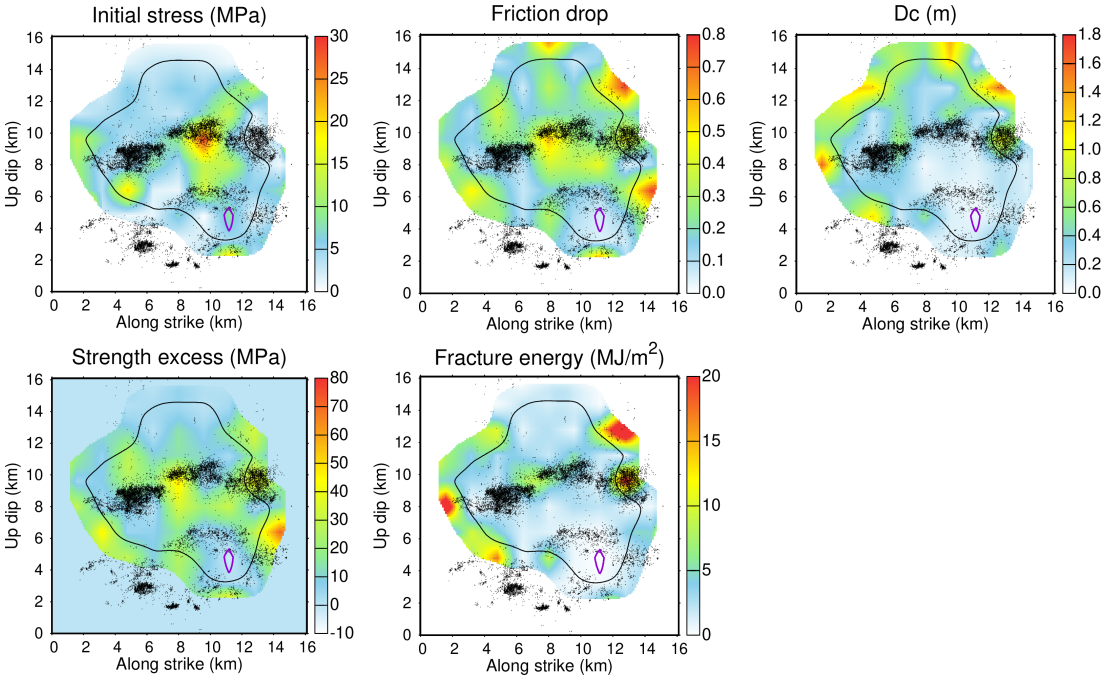


Figure 4.1 Distribution of the input dynamic parameters on the fault for the MAP rupture model. Black lines contour the region where the slip exceeds 10 % of the maximum slip value (slip contours), the purple line bounds the nucleation, and black dots denote foreshocks and aftershocks projected on the fault plane. Here, the fracture energy density G_F^{SW} was calculated using Eq. (2.20).

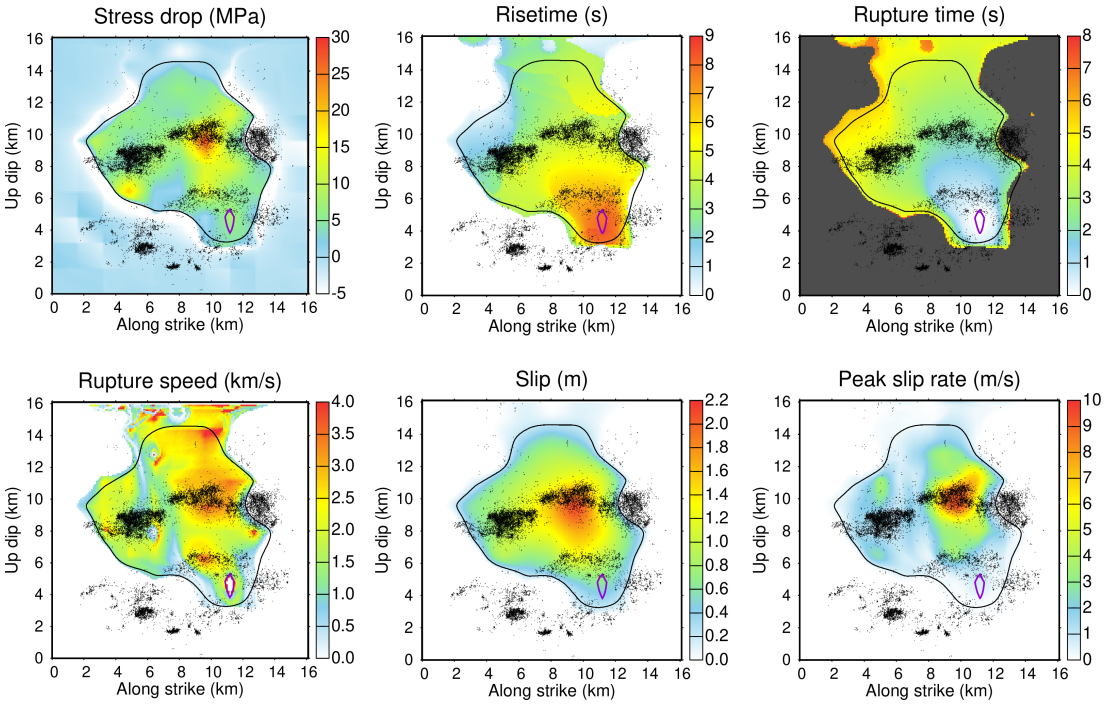


Figure 4.2 Distribution of the output rupture parameters on the fault plane for the MAP rupture model. Black lines contour the region where the slip exceeds 10 % of the maximum slip value, the purple line bounds nucleation, and black dots denote foreshocks and aftershocks projected on the fault plane.

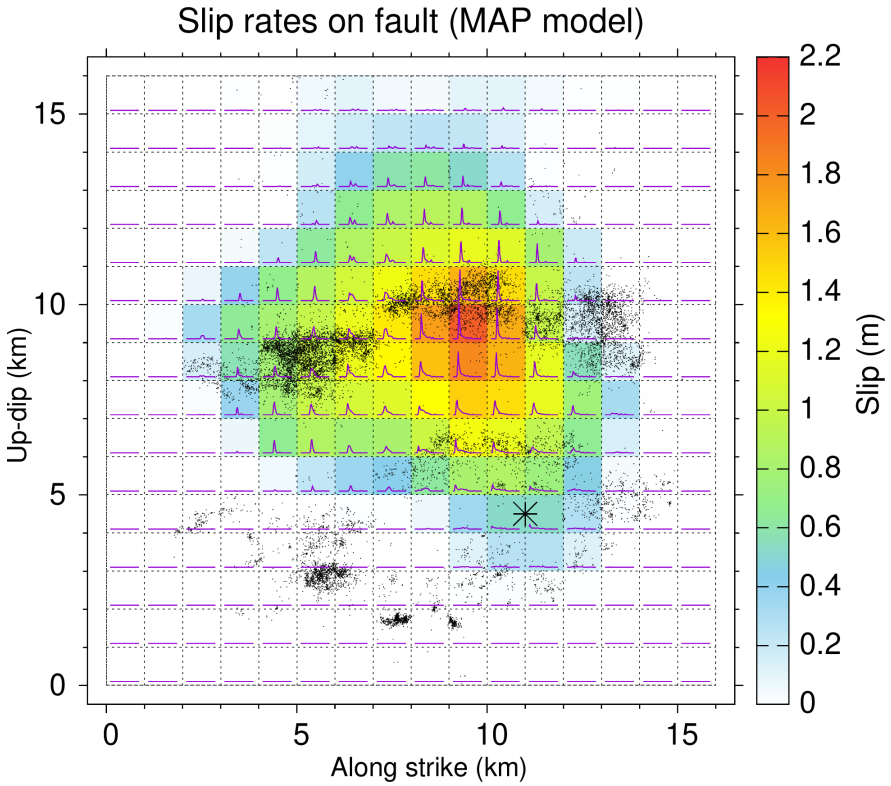


Figure 4.3 Slip distribution and slip rate functions (violet curves) on the fault (averaged over 1 km x 1 km subfaults). The black star denotes the position of the hypocenter, and the black dots are foreshocks and aftershocks projected on the fault plane.

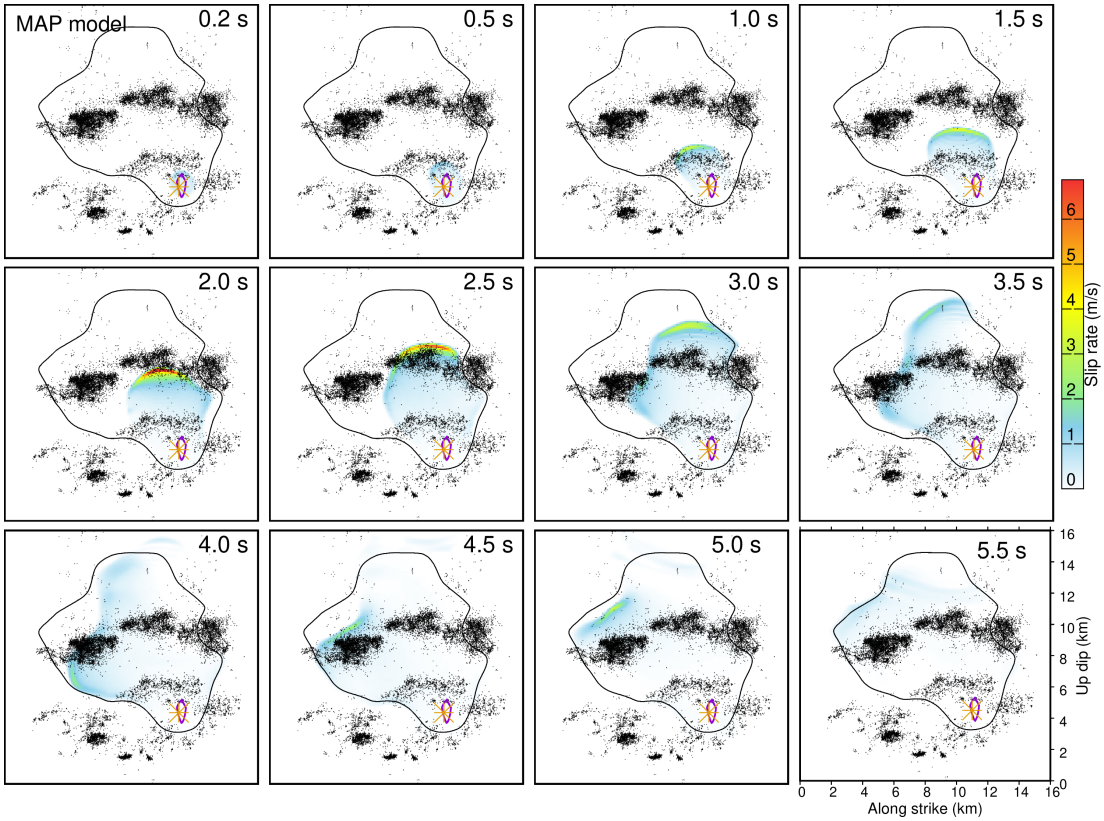


Figure 4.4 Temporal evolution of the horizontal component of slip rate on the fault for the MAP model. Black lines contour the region where the slip exceeds 10 % of the maximum slip value, violet line bounds nucleation, yellow star is the prescribed hypocenter position, and black dots denote foreshocks and aftershocks projected on the fault plane.

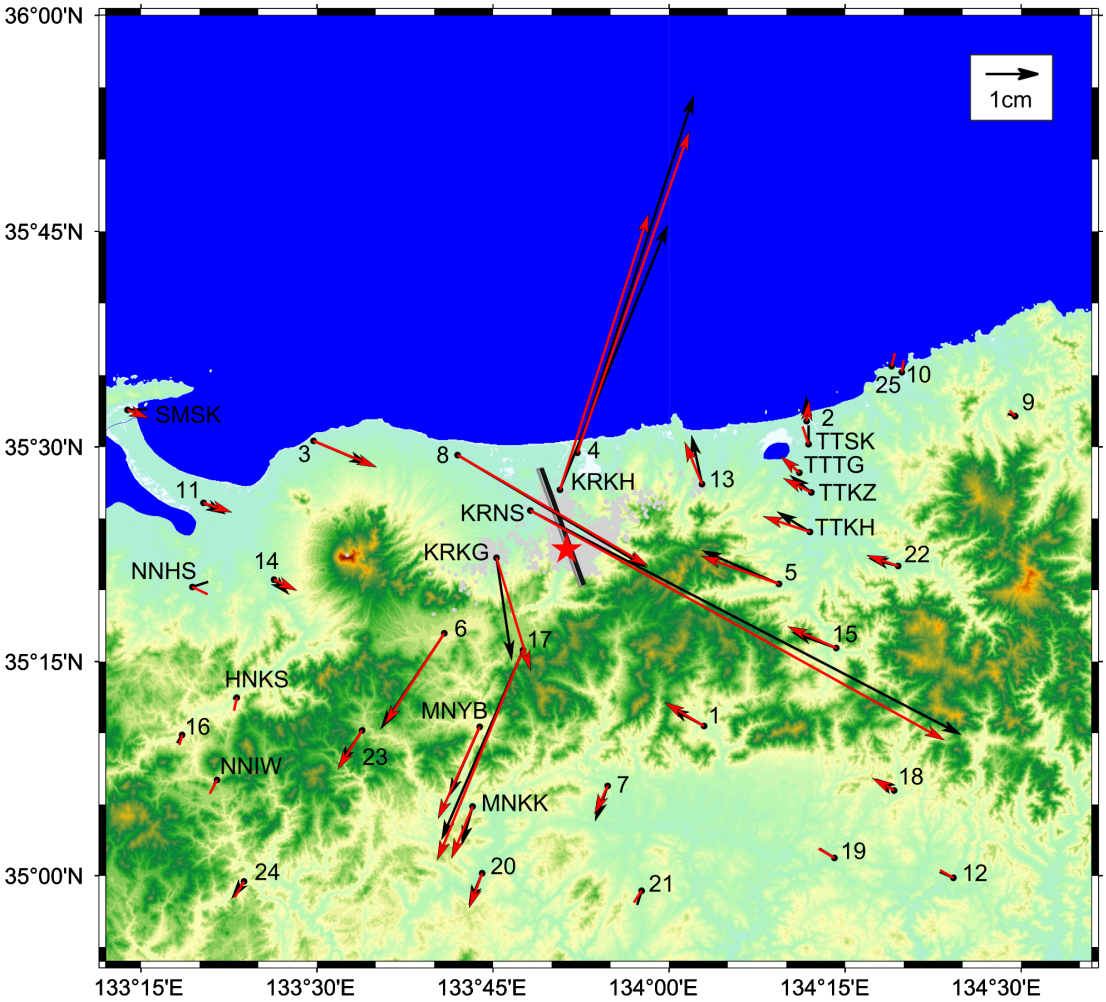


Figure 4.5 Observed (black) and synthetic (red) GNSS static displacements (scaled) for the MAP rupture model. The thick black and gray lines represent the surface projection of the lower and upper along-strike parts of the fault, the red star marks the epicenter location, and the gray dots indicate the positions of foreshocks and aftershocks.

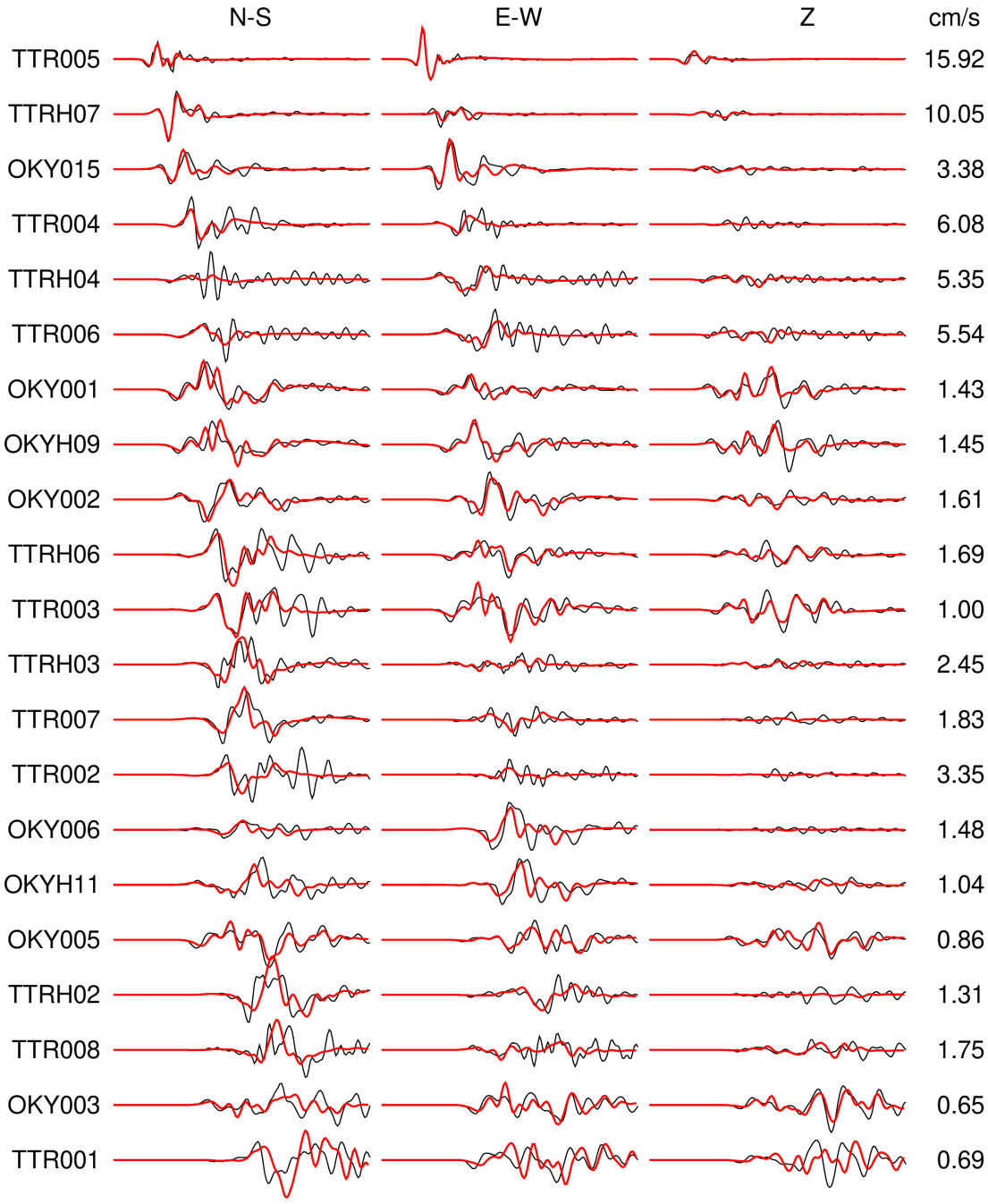


Figure 4.6 Comparison between observed (black) and synthetic (red) seismograms for the MAP rupture model. The left column lists the seismic station codes, followed by the three components: north-south, east-west, and vertical. The right column displays the amplitudes in cm/s. The duration of the recording is 30 seconds.

4.2 Ensemble models

In Figure 4.7 we show the slip contours for all accepted models in black-and-white colors according to their normalized PDF, together with the average and standard deviation. In Figure 4.8 and 4.9, we present the mean rupture parameters with their corresponding uncertainties of one sigma standard deviation plotted on the fault. The fault parameters are averaged over the ensemble of all accepted samples. We applied a mask to cover the area away from the average rupture, since parameters outside the rupture do not influence the calculation of synthetics and thus are not constrained by the data. In Figure 4.10 we present the moment rate functions of all accepted model samples in time in black and white according to their normalized PDF. Figure 4.11 shows inferred normalized histograms of parameters averaged over the fault with slip weighting and illustrates their dependencies on the misfit. The values of the mean parameters and standard deviations in terms of one sigma are listed in Table 4.2. The mean parameters are calculated using slip-weighted averaging over the fault. It gives more weight to better-constrained regions with higher slip.

The mean rupture area is $(85 \pm 12)\,\mathrm{km}^2$ and the mean slip is $(75.5 \pm 7.5)\,\mathrm{cm}$.

In the figure of the mean slip with its sigma standard deviation on the fault (Figure 4.9) we see a fairly elliptical area in the diagonal upward and NNW direction from the nucleation with quite high slip values reaching a maximum of 1.7 m and sigma being around 0.1-0.4 m. Within this region, the maximum slip tends to be concentrated in smaller areas, but with higher peak values; for example, see the results of the MAP model, which has a maximum value of 2.2 m (Figure 4.2). Next to this area in the northwest direction, we see a significant area with high sigma values of around 0.5 m. We can conclude that this region is not well constrained by the inversion, and individual models differ significantly there.

The average rupture duration in all ensembles is $(6.0 \pm 0.9)\,\mathrm{s}$, and from the moment rate functions (Figure 4.10) we can observe that after 6 seconds, the release of the seismic moment is already minimal in most models. The temporal evolution of the moment rate functions varies with asperities appearing at different times and with different intensities.

The rupture velocity distributions on the fault are heterogeneous in individual models; see the MAP model in Figure 4.2. The mean (slip-weighted and averaged over the fault and ensembles) rupture velocity $\overline{v_R}$ is $(2.10 \pm 0.12)\,\mathrm{km/s}$.

The stress drop distribution on the fault is heterogeneous both in the case of the mean value and the MAP model. Individual models tend to have large stress drop values along the vertical direction of rupture propagation from the hypocenter, at depths between 4 km and 11 km, however, we can see quite high variability between the models. Quite high values of sigma at the edges are partly caused by negative stress drop values near the rupture boundaries, but also because individual models differ there. In ensembles, we can see models with different locations of maximum stress drop. For example, some models with good misfit have a maximum of about 30 MPa at 3 km along strike and 8 km up dip, which we do not see in the mean value model because of the averaging. MAP model has a maximum of around 28 MPa at 10 km along strike and 10 km along dip.

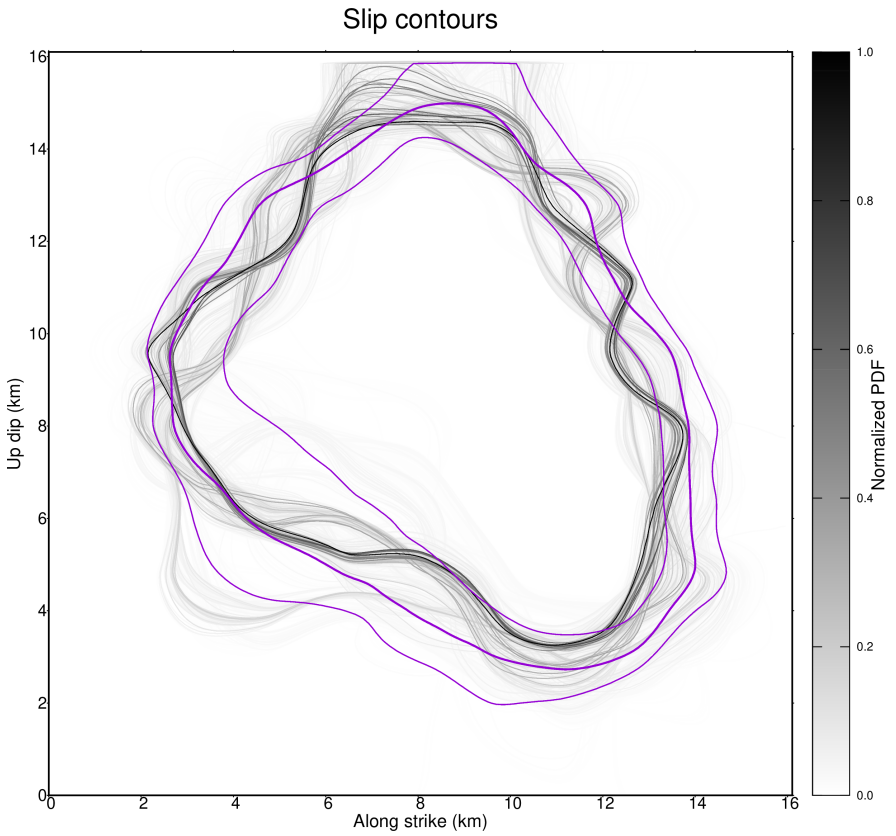


Figure 4.7 Slip contours on the fault for all accepted model samples. The gray scale represents the normalized probability density function (PDF). Thick violet lines indicate the contours of the mean model, while the two thin violet lines represent the averaged slip model with added and subtracted one-sigma uncertainty.

In the case of the MAP model, the dynamic parameter distribution on the fault was inhomogeneous (Figure 4.1). In Figure 4.8, the distribution is smoothed out due to averaging over the ensemble. The standard deviation is quite high, in some cases above 100 %. We can conclude that individual models diverge significantly here. It suggests a high variability of these parameters in the accepted models. The inferred mean prestress is (9.26 ± 1.34) MPa, mean strength excess is (14.05 ± 2.94) MPa and mean slip-weakening distance D_c is (32.58 ± 5.73) cm. In histograms (Figure 4.11), we can see that the ranges of these parameters are quite wide across the ensembles.

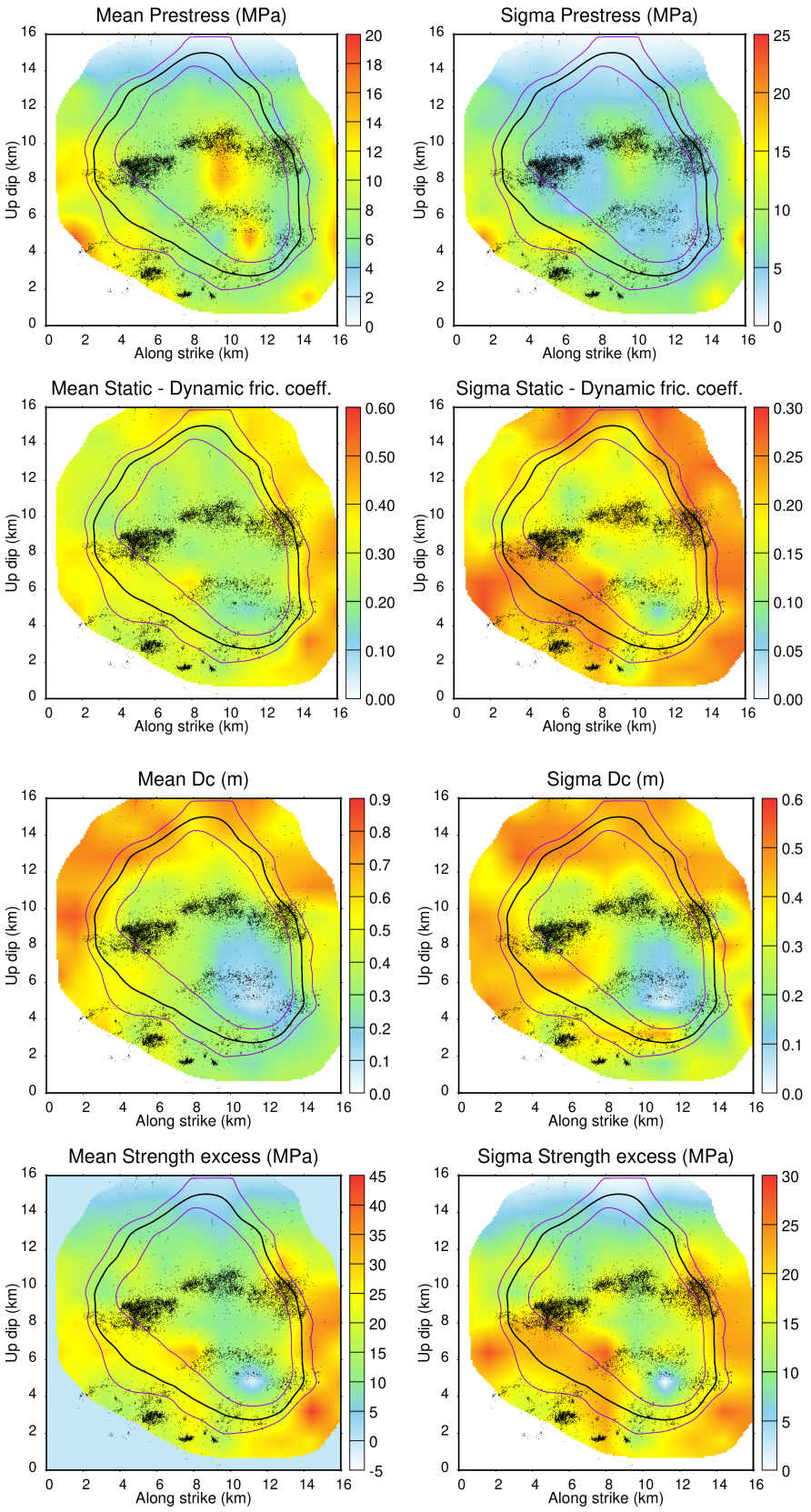


Figure 4.8 Mean input model parameters on the fault (averaged over the ensemble models) with their uncertainties in terms of one sigma, as inferred by the Bayesian dynamic rupture inversion. Black and violet curves outline the contours of the mean slip model with one sigma uncertainties, respectively. Black dots denote the position of the aftershocks and foreshocks.

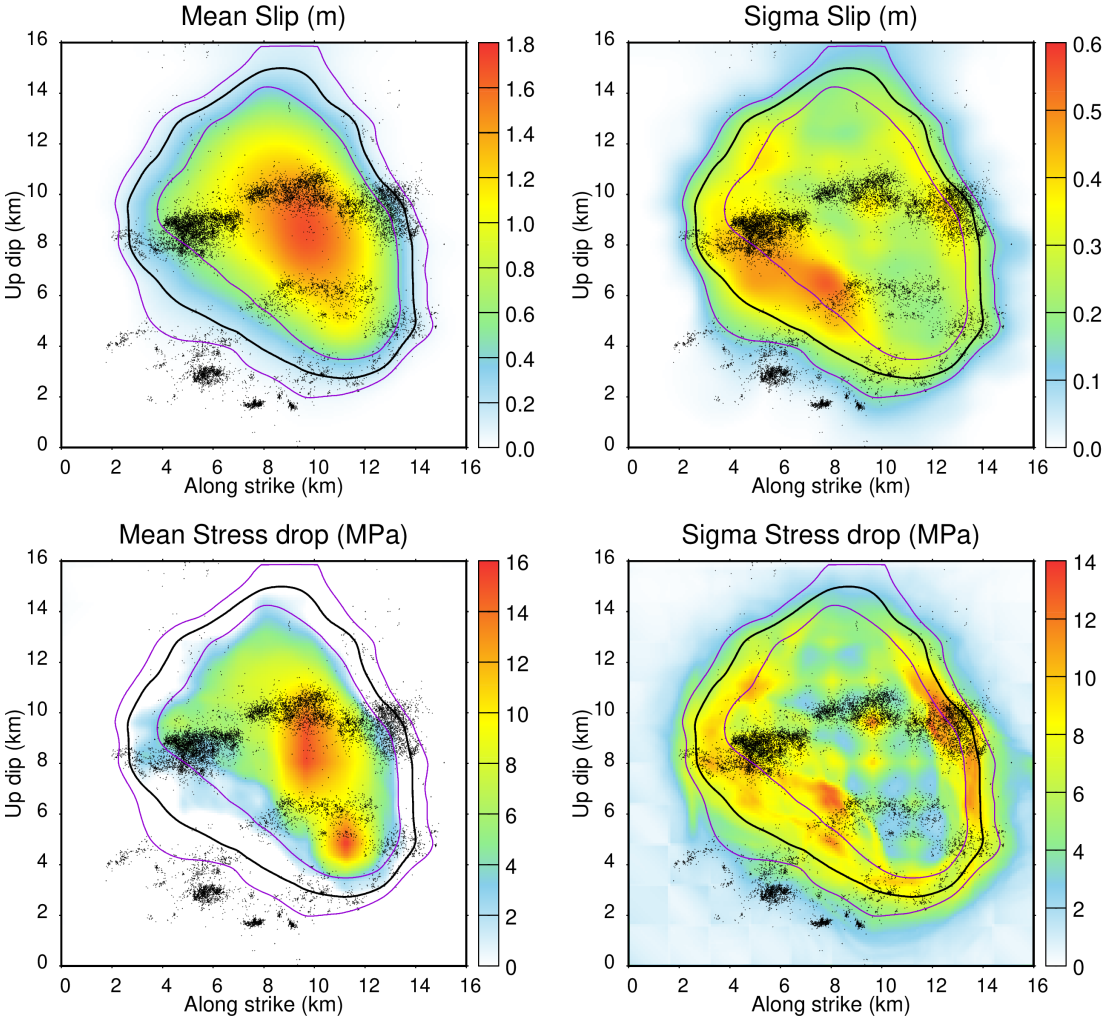


Figure 4.9 Mean output model parameters on the fault with their uncertainties in terms of one sigma, as inferred by the Bayesian dynamic rupture inversion. Black and violet curves outline the contours of the mean slip model with one sigma uncertainties, respectively. Black dots denote the position of the aftershocks and foreshocks.

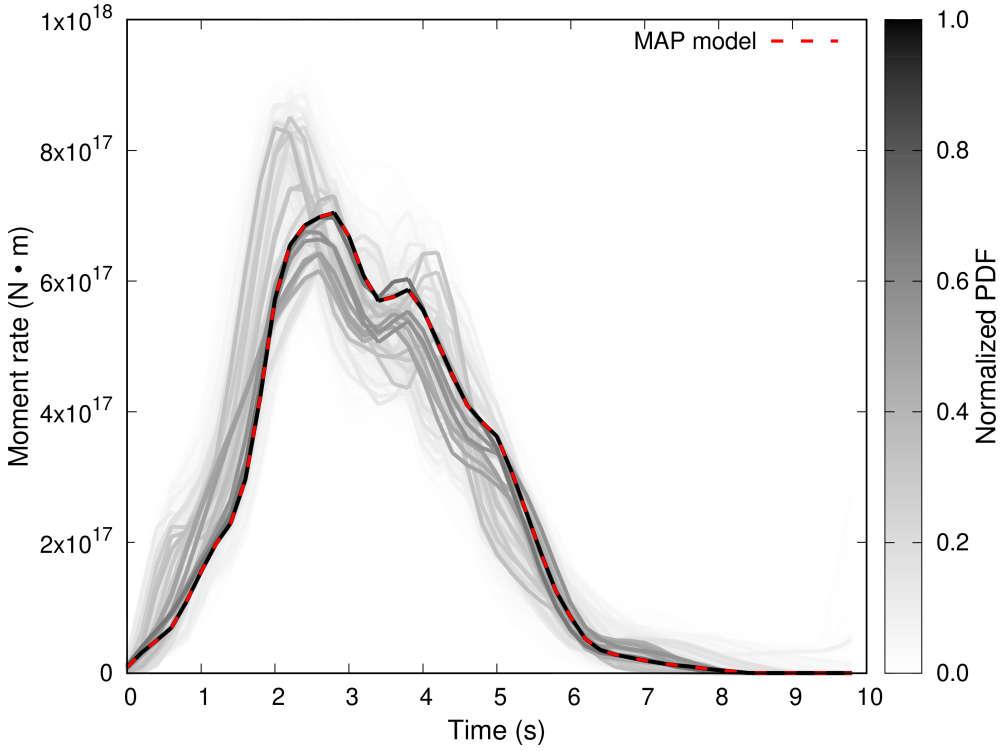


Figure 4.10 Moment rate functions over time for all accepted model samples. The gray scale represents the normalized probability density function (PDF), and the red dashed line indicates the maximum a posteriori (MAP) model.

Parameter	**Mean ± Standard Deviation**
Misfit	57.66 ± 3.90
Seismic VR [%]	46.22 ± 3.39
Seismic moment M_0 [10^{18} Nm]	2.47 ± 0.25
Mean stress drop $\overline{\Delta T}$ [MPa]	8.80 ± 1.58
Fracture energy E_F [10^{14} J]	3.06 ± 0.57
Fracture energy Density G_F [MJ/m^2]	3.70 ± 1.13
Radiated energy E_R [10^{13} J]	4.18 ± 0.79
Radiation efficiency η_{rad} [%]	12.15 ± 1.92
Scaled energy ϵ_R [$\times 10^{-5}$]	1.71 ± 0.35
Stress level SL [MPa]	0.44 ± 0.03
Mean strength T_S [MPa]	23.31 ± 4.28
Mean strength Excess $(T_s - T_i)$ [MPa]	14.05 ± 2.94
Mean slip-weakening distance D_c [cm]	32.58 ± 5.73
Mean slip s [m]	75.46 ± 6.51
Rupture area A_R [km^2]	85.46 ± 12.27
Mean rupture velocity $\overline{v_R}$ [km/s]	2.10 ± 0.12
Rupture duration [s]	6.00 ± 0.88
Nucleation zone size [km^2]	0.23 ± 0.14
Mean nucl. overstress [MPa]	0.79 ± 0.14
Nucl. center along strike x_0 [km]	11.20 ± 0.14
Nucl. center along dip z_0 [km]	4.87 ± 0.09

Table 4.2 Values of the inferred mean parameters and standard deviations in terms of one sigma. Mean parameters are calculated using slip-weighted averaging over the fault and averaging over the ensembles.

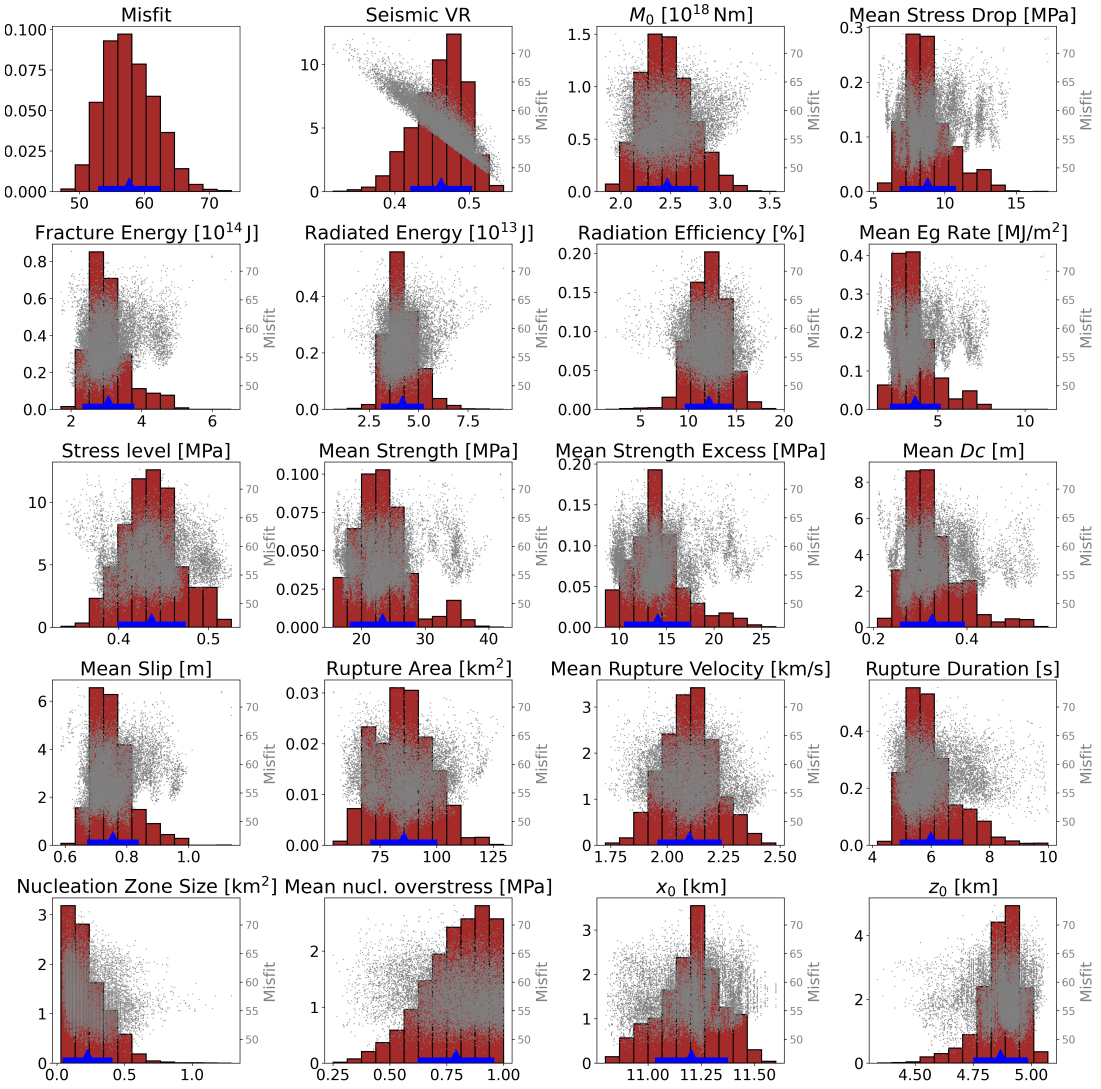


Figure 4.11 Normalized histograms of the kinematic and dynamic rupture parameters inferred by the Bayesian dynamic rupture inversion. Gray dots denote the misfit values. Mean parameters are slip-averaged over the fault. Blue triangles and lines are the mean values over the ensembles with their one sigma standard deviation intervals (see Table 4.2).

5 Discussion

5.1 Comparison to published papers

Our inferred rupture areas are larger and have lower slip values than those of Ross et al. (2018). The main slip distribution is not as deep and concentrated around the hypocenter as in Ross et al. (2018) and Shibata and Aso (2025), and is not as shallow as in Amey et al. (2019). The distribution is quite similar to Meneses-Gutierrez et al. (2019).

Several scenarios fit the measured data with comparable reliability; see the slip contours and their corresponding probability density functions (PDFs) in Figure 4.7. The rupture extends to depths of approximately 12.5 to 14 km. In some cases, the rupture reaches the free surface. However, we can conclude that the slip values there are rather small. Therefore, fault parts above a depth of 1 km likely do not contribute significantly to the fit of the coseismic data. Meneses-Gutierrez et al. (2019) concluded that the shallow slip is primarily caused by the postseismic phase and that the coseismic slip does not occur at depths shallower than 1 km. This is consistent with our results. Specifically, in the case of the MAP model, we observe very small near-surface slip.

Kubo et al. (2017) observes two asperities, one larger located in the hypocenter and one smaller in the NNW direction. We see some similarities in the distribution of peak slip rate on the fault; see Figure 4.2, there are also two main asperities with quite similar shapes.

The mean (slip-weighted) stress drop is (8.8 ± 1.6) MPa, which is less than the stress drop of $18 - 27$ MPa calculated by Ross et al. (2018). This discrepancy is due to our larger rupture area.

The value of our inferred scalar seismic moment with one sigma uncertainty $(2.47 \pm 0.25) \times 10^{18}$ Nm seems smaller than results of GCMT (Ekström et al., 2012) 2.91×10^{18} Nm and result of U.S. Geological Survey (2025) 2.82×10^{18} Nm, but we can see that the histogram covers these values (Figure 4.11). The inverted value differs significantly across published articles, however they are within or close to our mean interval with one sigma; 2.54×10^{18} Nm by Ross et al. (2018), 2.15×10^{18} Nm by Meneses-Gutierrez et al. (2019), 2.1×10^{18} Nm by Kubo et al. (2017), 2.4×10^{18} Nm by Liu et al. (2019) and $(2.6 - 2.92) \times 10^{18}$ Nm by Amey et al. (2019).

Our radiated energy $(4.18 \pm 0.79) \times 10^{13}$ J is between the two values 2.0×10^{13} J and 5.5×10^{13} J inferred by IRIS (Incorporated Research Institutions for Seismology) (2025) for high (0.5-2 s) and broadband (0.5-70.0 s) frequency range , respectively. It is slightly smaller than the result of Ross et al. (2018) $(5.75 - 12.2) \times 10^{13}$ J, who calculated the seismic energy from the STF spectra and used the omega-square Brune model to correct for the missing energy.

The radiation efficiency is quite low, (12.15 ± 1.92) %, which is a sign that the Tottori 2016 earthquake was highly dissipative. Approximately 90% of the energy was consumed for the propagation of the rupture, and only approximately

10% was radiated in the form of seismic waves. Ross et al. (2018) calculated the radiation efficiency using stress drop, seismic moment, and radiated energy, which resulted in values even lower than ours, in the range of $(5.1 - 7.7)\%$.

Our moment scaled energy ϵ_R is $(1.71 \pm 0.35) \times 10^{-5}$, which is less than the value of Ross et al. (2018) (2.3×10^{-5}).

5.2 Variability of rupture parameters within the ensemble

We randomly selected models from the ensemble and created animations of the distributions of the rupture parameters on the fault. Videos of these animations are included as attachments. The descriptions of the individual snapshots are the same as those in Figures 4.1 and 4.2. To illustrate the variability of models, in Figures 5.1 and 5.2 we show the slip and stress drop distributions, respectively, of six selected rupture models from the ensemble.

As mentioned above, ruptures vary in size, shape, magnitude of slip, and location on the fault. The size range is quite wide, from 50 to 125 km^2, with a mean of (86 ± 12) km^2. As was shown in the previous section, the size of the rupture influences the magnitude of some parameters, i.e., larger ruptures tend to have a lower mean slip and a lower mean stress drop. The distributions of the parameters on the fault vary both in spatial extent and magnitude. The dynamic parameters are more heterogeneous than the kinematic parameters, so the uncertainty of the dynamic parameters is usually larger. The large uncertainties are due to the non-uniqueness of this inverse problem and the limited frequency range of the data (Gallovič et al., 2019a).

Slip distributions differ across the ensemble, although not so much as the dynamic parameters. They are also less heterogeneous. The maximum slip, ranging from approximately 1.6 to values above 2.2 meters, typically occurs within the main rupture path in the up-dip north-west direction from the hypocenter, within the area of the mean slip model minus one sigma uncertainty; see Figure 4.7. This area is the most constrained by the inversion. Within this area, the uncertainties of almost all parameters are relatively lower.

The distribution of the stress drop varies more between the ensembles than in the case of slip. The maximum appears in different locations with magnitudes ranging from about 15 to 30 MPa. Some of these locations are not visible in the mean value model (Figure 4.9), and we can only observe larger uncertainties.

The rupture velocity is quite heterogeneous (e.g., see the MAP model in Figure 4.2), and its spatial distribution differs quite a lot in the ensemble. In almost all models, we observe a significant rise time around the nucleation.

In the case of the dynamic parameters, we observe high variability among the ensemble. Individual models are heterogeneous, with maxima appearing at different locations with different amplitudes. For example, some models have a maximum prestress of 30 MPa, while others have a maximum of about 20 MPa.

A similar pattern is observed for the friction drop, greater than 0.9 versus approximately 0.4, and for D_c, approximately 1.8 m versus 0.6 m. As we mentioned previously, the mean model values on the fault (Figures 4.8 and 4.9) are smoothed out by averaging the individual models from the ensemble. Therefore, the maxima of the rupture parameters in the mean model are much smaller (about 20 MPa for prestress, about 0.6 for friction drop, and about 0.9 m for D_c) than the maxima in individual models.

In the mean model, the lowest mean prestress values, the highest mean D_c, and the mean strength excess values occur at the edges of the rupture. These are the features capable of arresting the rupture propagation. However, the associated parameters in these areas exhibit large uncertainties. Consequently, the rupture arrest mechanism varies locally along the fault and between individual models.

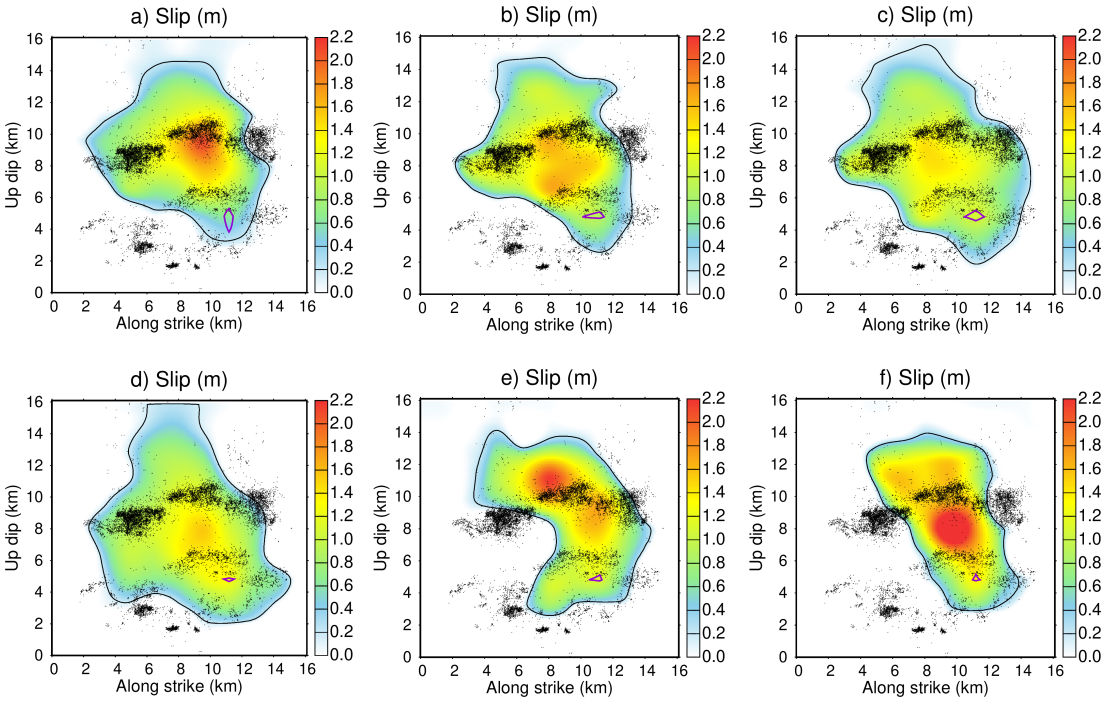


Figure 5.1 Slip distribution on the fault for six randomly selected rupture models from the ensemble. Black lines contour the region where the slip exceeds 10 % of the maximum slip value, the purple line bounds nucleation, and black dots denote foreshocks and aftershocks projected on the fault plane. The MAP is in the subplot a).

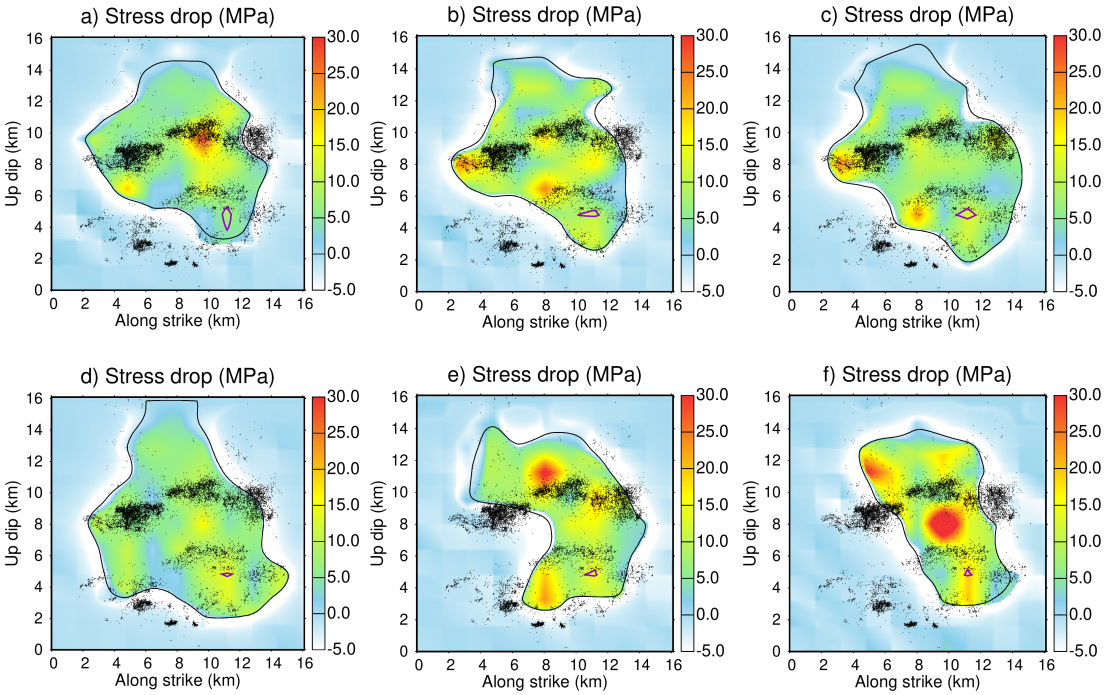


Figure 5.2 Stress drop distribution on the fault for six selected rupture models from the ensemble. Black lines contour the region where the slip exceeds 10 % of the maximum slip value, the purple line bounds nucleation, and black dots denote foreshocks and aftershocks projected on the fault plane. The MAP is in the subplot a).

5.3 Slip-weakening distance vs distance from the nucleation

Andrews (2005) investigated energy loss in a damage zone surrounding a dynamically propagating rupture front during an earthquake. The damage zone is a material area surrounding the principal slip zone where off-fault inelastic deformation occurs due to high stress concentrations near the dynamically propagating rupture front. In Andrews (2005), the material in the damage zone is governed by a Coulomb yield criterion. He found that in his model, energy loss in the damage zone contributes significantly to the energy budget. He formally included this off-fault loss in the on-fault fracture energy and showed that it increases linearly with the rupture propagation distance and becomes much larger than the energy dissipated on the fault itself by the constitutive frictional law.

By applying the slip velocity function obtained from the non-elastic calculation as a boundary condition on a fault in an elastic medium, Andrews (2005) derived the corresponding shear stress evolution in an equivalent elastic problem. The resulting stress-slip curves exhibit slip-weakening behavior. The breakdown slip-weakening distance D_c scales linearly with rupture propagation distance. Furthermore, the elastic fracture energy matches the off-fault fracture energy in the non-elastic calculation.

Here, we examine whether D_c and G_F exhibit behavior similar to that described above. In the initial model (Figure 3.4), we prescribed a linear increase in D_c with distance from the nucleation point to maintain an approximately constant rupture

velocity. Then, we ran the inversion, with the MCMC chains randomly perturbing the model parameters to explore the model space and minimize the misfit. The resulting models still show a linear increase in D_c with distance. Indeed, Figure 5.3 shows that the mean D_c increases linearly with the distance from the nucleation center, with a Pearson product-moment correlation coefficient value of 0.91. In the case of the MAP model, the values have a broader range; however, we can still observe a slightly increasing trend with the correlation coefficient of 0.67.

If we average these values over the radius distance from the nucleation center R, the linear trend is even more pronounced; see Figure 5.4. In this case, the Pearson correlation coefficients are 0.99 and 0.97 for the mean model values and the MAP model values, respectively.

A similar relationship is obtained for the fracture energy density as a function of distance from the nucleation center; see Figure 5.5. For this analysis, we only used values within 6 km of the nucleation center and with slip exceeding 20 % of the maximum slip. This restriction was applied because values at greater distances effectively decrease to zero by definition. The correlation coefficients are 0.99 and 0.98 for the mean values and MAP models, respectively.

We suggest that the linear increase in (apparent) D_c and G_F from the hypocenter can be interpreted as an apparent feature that substitutes for the effect of (unmodeled) significant off-fault yielding. The distance-dependent D_c may be interpreted as a proxy parameter for energy dissipation occurring outside the principal slip zone. However, further analysis and interpretation are needed.

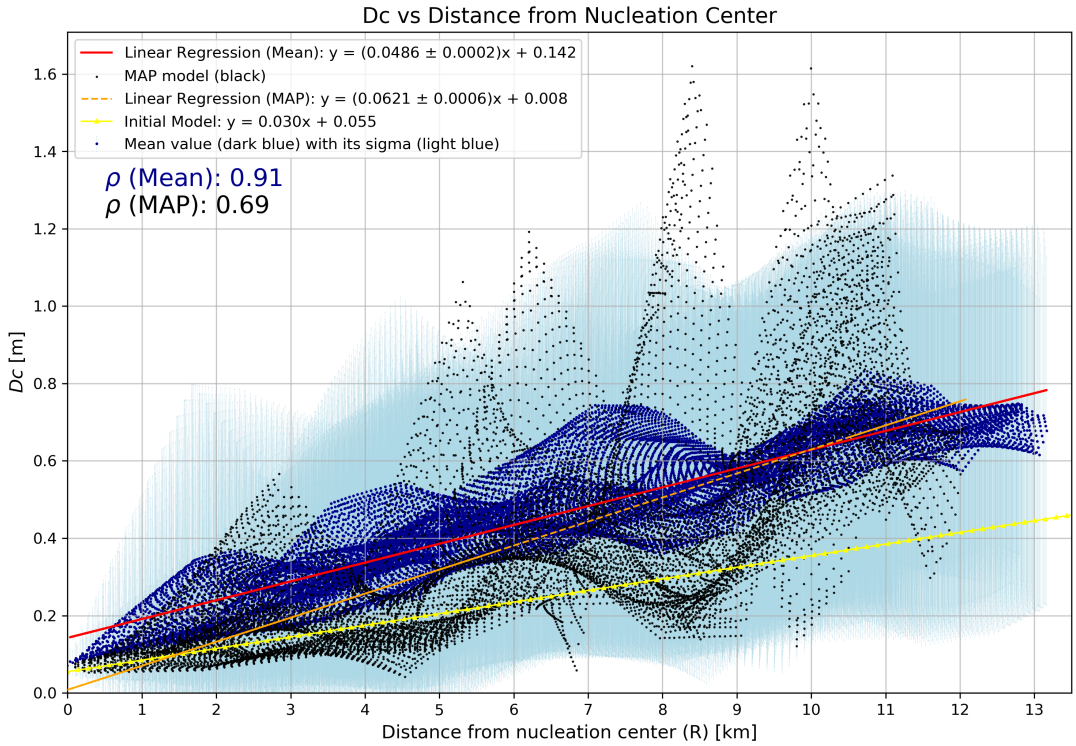


Figure 5.3 D_c shown as a function of the distance from the nucleation center. Dark blue dots represent the ensemble-averaged mean D_c values with respect to the mean nucleation center, with its corresponding sigma uncertainty interval shown as light blue lines. Black dots indicate the MAP model D_c values with respect to the MAP nucleation center. Red and orange lines denote the linear regressions of the mean and MAP models, respectively. The initial model relationship is indicated by the yellow line. The correlation coefficient ρ is the Pearson product-moment correlation coefficient.

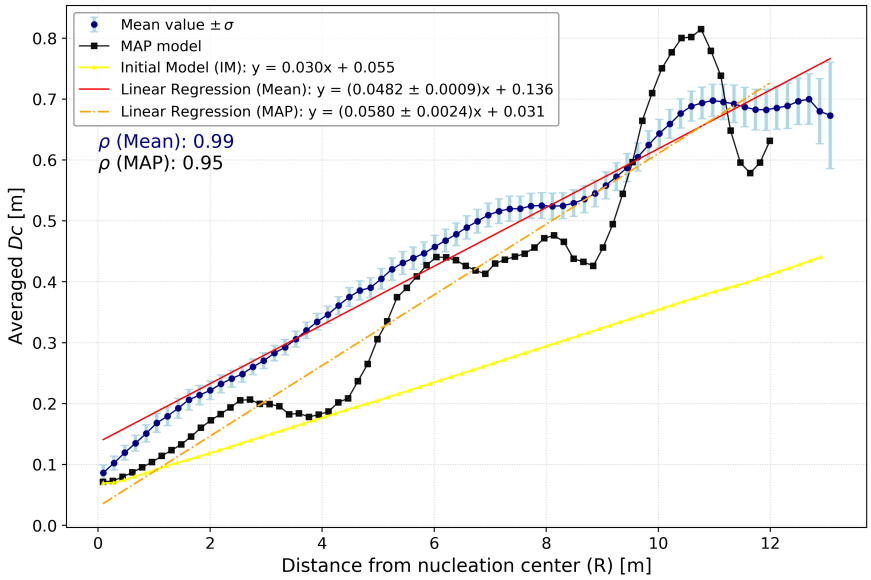


Figure 5.4 Averaged D_c values over the specified annulus for the mean (blue), MAP (black), and initial model (yellow). The values are fitted with linear regression lines (see legend). The correlation coefficient ρ is the Pearson product-moment correlation coefficient.

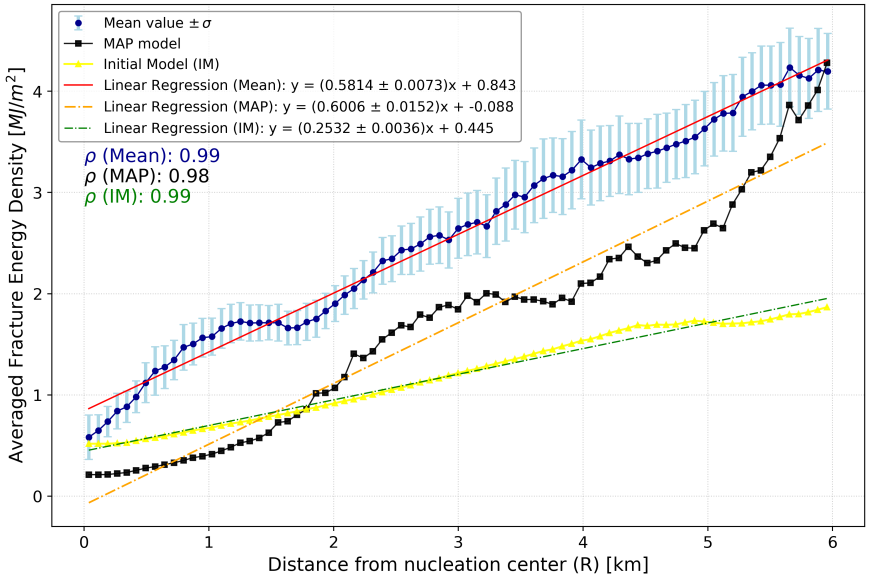


Figure 5.5 Values of fracture energy density G_F averaged over the specified annulus for the mean (blue), MAP (black), and initial model (yellow). The values are fitted with linear regression lines (see legend). The correlation coefficient ρ is the Pearson product-moment correlation coefficient.

5.4 Parameters correlations, and trade-offs

We evaluated the Pearson product-moment correlation coefficient between 20 inferred parameters; see Figure 5.6. The heatmap trade-offs between selected inferred parameters, with the respective Pearson product-moment correlation coefficient, can be found in Figure 5.7.

A strong anticorrelation is found between mean stress drops and rupture areas ($\rho = -0.85$). This is likely due to constraints on the seismic moment. From the histograms with the corresponding misfit (Figure 4.11), we can see that the seismic moment is quite well constrained. In other words, on average, if we increase the mean stress drop, we need to decrease the rupture area to keep the seismic moment approximately constant. This is in agreement with the commonly used scaling relationship between seismic moment M_0, stress drop ΔT, and rupture length L (or area A_R), for example, see Somerville (2021): $M_0 \propto \Delta T\ L^3 \propto \Delta T A_R^{2/3}$.

We also see a decreasing trend between the rupture area and mean slip ($\rho = -0.46$). The anticorrelation is again not perfect, although it could be expected due to the well-constrained seismic moment, and the theory (Equation 2.27).

Our results also show that models with larger slip tend to prefer a higher stress release. The correlation coefficient between the mean stress drop and the mean slip is $\rho = 0.75$. Note that we do not see perfect correlations because other factors (i.e., spatial heterogeneity, frictional properties, energy dissipation, and impacts of simplified linear fracture mechanics) influence these relationships.

There is a high correlation between the mean stress drop and the mean E_g rate ($\rho = 0.98$). From Figure 4.11 we can see that the rupture velocity is quite well constrained. A plausible interpretation is that an increase in stress drop is

compensated by higher fracture energy to slow down the rupture propagation to keep the rupture velocity in a narrow range (from about 1.9 km/s to 2.2 km/s).

The rupture is expected to be faster if it spends less energy to advance the crack front (Kanamori and Rivera, 2006). In our results, we can see that the mean rupture velocity increases with increasing radiation efficiency with a coefficient $\rho = 0.64$.

The fracture energy rate E_g is calculated from the strength and D_c (Equation (2.33)). This is the reason why we see strong correlations between the mean E_g rate and the mean strength ($\rho = 0.92$) and the mean D_c ($\rho = 0.81$). It is also negatively correlated with the rupture area ($\rho = -0.79$). On average, increasing the mean fracture energy density (or D_c) tends to stop the rupture earlier and reduces the rupture area.

The 2D crack tip equation of motion suggests that the rupture growth is primarily controlled by the stress drop ΔT, and fracture energy rate $E_g = (T_s - T_d)D_c/2$, while weakening rate $W = (T_s - T_d)/D_c$ plays a secondary role, and thus suggests $T_s \sim 1/D_c$. Gallovič et al. (2019a) tested this idea and investigated the trade-off between D_c and strength. They found a weaker anticorrelation than expected from the aforementioned theory ($T_s \sim 1/D_c^{0.27}$). Instead, our results show a moderate positive correlation ($\rho = 0.58$), suggesting that roughly $T_s \sim D_c$, and therefore the inversion is at least partially sensitive to the weakening rate.

We can conclude that the data are quite sensitive to the seismic moment and the rupture velocity. However, the trade-offs between parameters are not always trivial, and there are more factors influencing the relationships.

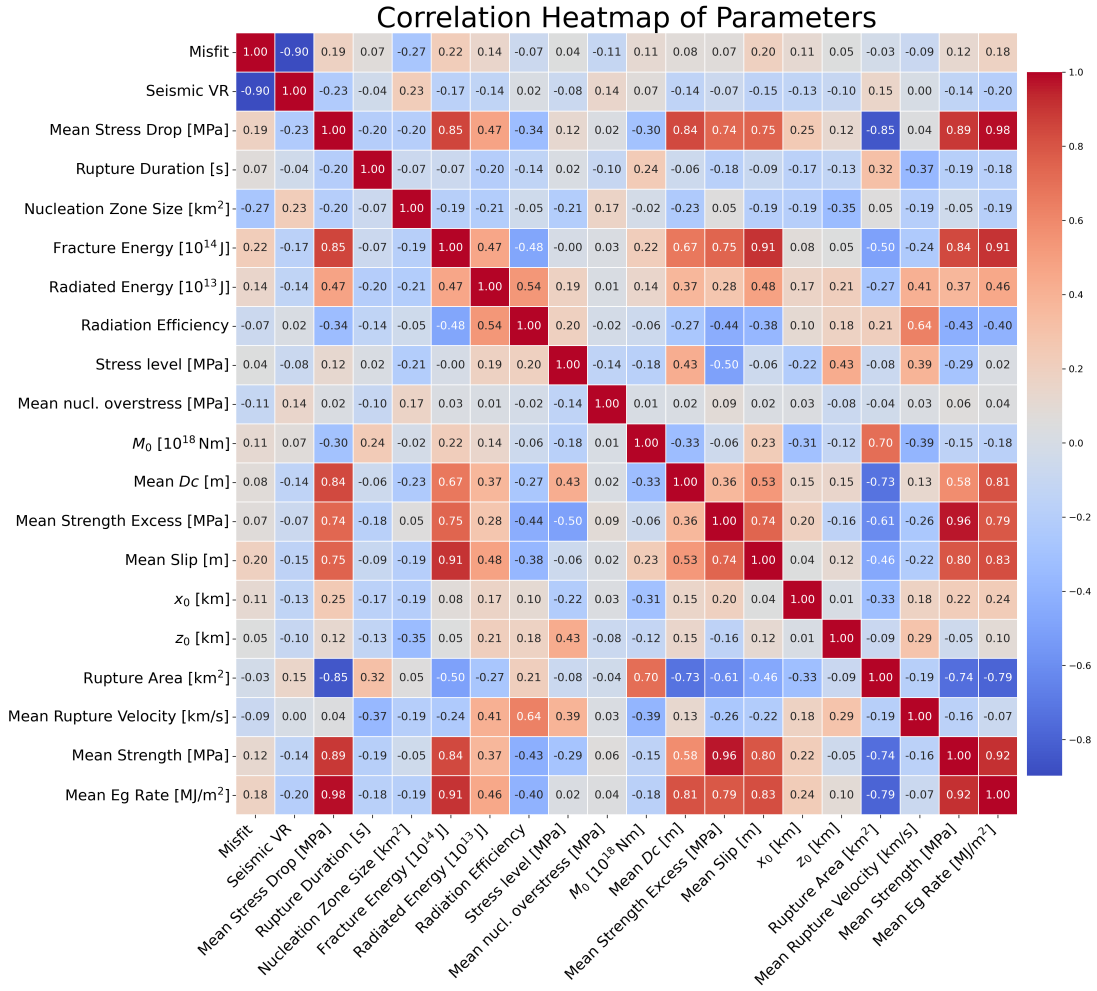


Figure 5.6 Correlation heatmap of inferred parameters. The number is the Pearson product-moment correlation coefficient. Mean parameters are slip-averaged. Parameters are introduced in Section 2.1.3 and 2.1.5. x_0 and z_0 denote the mean nucleation center along the strike and up the dip.

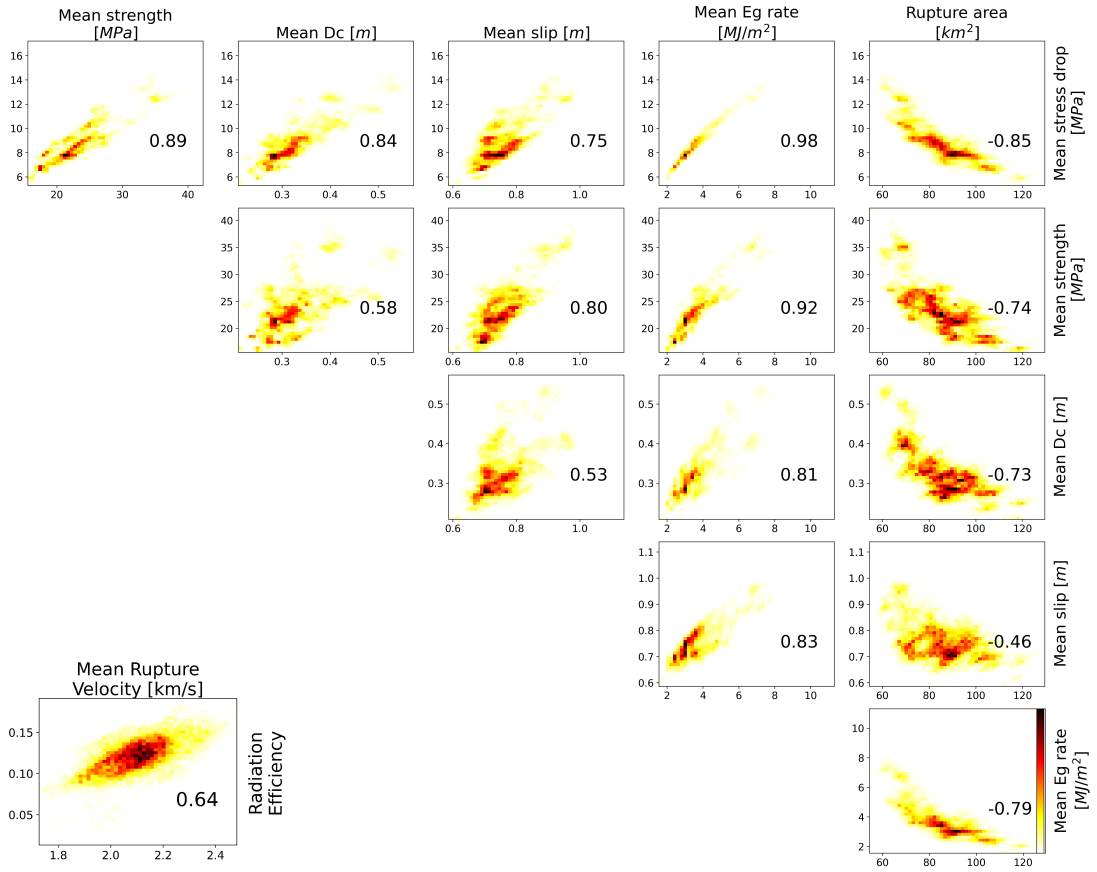


Figure 5.7 The relationship between selected inferred parameters, with the respective Pearson product-moment correlation coefficient (black number in the subplot). Mean parameters are slip-averaged. Parameters are introduced in Section 2.1.3 and 2.1.5.

5.5 Foreshocks and aftershocks

In this study, we used foreshocks and aftershocks that were relocated by Ross et al. (2018). They found that the main slip area is surrounded by aftershocks. In contrast, we observe no clear correlation or anticorrelation between the distribution of foreshocks and aftershocks and slip, or other rupture parameters. In Figures 5.1 and 5.2, we illustrate this on the six selected models from the ensemble. We only plotted the seismicity within two kilometers of the fault plane. As we can see, in some models, the rupture covers most of the aftershock locations, and thus the relationship between the aftershocks and the slip (or stress drop) distribution is elusive.

Conclusion

In this thesis, we conducted a so-far missing dynamic source inversion of the 2016 Mw 6.2 Central Tottori earthquake using low-frequency seismic waveforms and GNSS static coseismic displacements. We obtained an ensemble of models with complex rupture propagation. We found that many different scenarios of rupture evolution explain the observed data with similar reliability.

We compared our results with previously published kinematic inversions. The main slip distribution is neither as deep nor as focused around the hypocenter as in the results of Ross et al. (2018) and Shibata and Aso (2025), nor as shallow as that presented by Amey et al. (2019). Rather, it closely resembles the distribution obtained by geodetic inversion in Meneses-Gutierrez et al. (2019).

The mean model reveals the main slip area in the NNW and up-dip direction from the nucleation extending from depths of about 12 to 2 km. Within this area, individual models of the ensemble tend to reach their maximum slip values. Within this main rupture path, both the kinematic and dynamic parameters have smaller uncertainties and are better constrained by the inverse problem. We also identify the region that is not so well constrained, where the slip and almost all other parameters have large uncertainties.

We found that the distributions of the dynamic parameters on the fault are quite heterogeneous and vary significantly between models in the ensemble, resulting in large uncertainties in the model parameters. The large uncertainties are due to the non-uniqueness nature of the inverse problem and the limited frequency range of the data. We found no clear relationship between the distribution of foreshocks or aftershocks and slip or other rupture parameters. We discussed the correlations and trade-offs among the kinematic and dynamic rupture parameters. We concluded that the data are most sensitive to the seismic moment and the rupture velocity, although the trade-offs are not always straightforward, and there are more factors influencing the relationships.

We find that the slip-weakening distance and the fracture energy density increase on average linearly with distance from the hypocenter, and suggest that this can be interpreted as an apparent feature substituting the effect of (unmodeled) significant off-fault yielding.

In future research, we suggest extending the inversion to higher frequencies to extract more detailed information about the source and better constrain the inverse problem. This would require adding smaller-scale heterogeneities to the dynamic parameter distributions on the fault, which is uneasy and requires, e.g., 3D Green's functions and a precise velocity model.

Bibliography

Aki, K. and P. G. Richards (2002). *Quantitative Seismology*. 2nd ed. Sausalito, CA: University Science Books. ISBN: 0935702962. URL: http://www.worldcat.org/isbn/0935702962.

Amey, R. M. J., A. Hooper, and Y. Morishita (Apr. 2019). "Going to Any Lengths: Solving for Fault Size and Fractal Slip for the 2016, Mw 6.2 Central Tottori Earthquake, Japan, Using a Transdimensional Inversion Scheme". en. In: *Journal of Geophysical Research: Solid Earth* 124.4, pp. 4001–4016. DOI: 10.1029/2018jb016434. URL: http://dx.doi.org/10.1029/2018JB016434.

Ampuero, Jean Paul et al. (2024). *jpampuero/sem2dpack: SEM2DPACK v2.3.9*. Zenodo. DOI: 10.5281/ZENODO.13821494. URL: https://zenodo.org/doi/10.5281/zenodo.13821494.

Andrews, D. J. (Nov. 1976). "Rupture velocity of plane strain shear cracks". en. In: *Journal of Geophysical Research* 81.32, pp. 5679–5687. DOI: 10.1029/jb081i032p05679. URL: http://dx.doi.org/10.1029/JB081i032p05679.

— (Jan. 2005). "Rupture dynamics with energy loss outside the slip zone". en. In: *Journal of Geophysical Research: Solid Earth* 110.B1. DOI: 10.1029/2004jb003191. URL: http://dx.doi.org/10.1029/2004JB003191.

Barall, Michael (Aug. 2009). "A grid-doubling finite-element technique for calculating dynamic three-dimensional spontaneous rupture on an earthquake fault". en. In: *Geophysical Journal International* 178.2, pp. 845–859. DOI: 10.1111/j.1365-246x.2009.04190.x. URL: http://dx.doi.org/10.1111/j.1365-246X.2009.04190.x.

Cotton, Fabrice and Olivier Coutant (Mar. 1997). "Dynamic stress variations due to shear faults in a plane-layered medium". en. In: *Geophysical Journal International* 128.3, pp. 676–688. DOI: 10.1111/j.1365-246x.1997.tb05328.x. URL: http://dx.doi.org/10.1111/j.1365-246X.1997.tb05328.x.

Dalguer, Luis A. and Steven M. Day (Feb. 2007). "Staggered-grid split-node method for spontaneous rupture simulation". en. In: *Journal of Geophysical Research: Solid Earth* 112.B2. DOI: 10.1029/2006jb004467. URL: http://dx.doi.org/10.1029/2006JB004467.

Earth Science, National Research Institute for and Disaster Resilience (2019). *NIED K-NET, KiK-net*. DOI: 10.17598/nied.0004. URL: https://doi.org/10.17598/nied.0004.

Ekström, G., M. Nettles, and A.M. Dziewoński (2012). "The global CMT project 2004–2010: Centroid-moment tensors for 13,017 earthquakes". en. In: *Physics of the Earth and Planetary Interiors* 200–201, pp. 1–9. DOI: 10.1016/j.pepi.2012.04.002. URL: http://dx.doi.org/10.1016/j.pepi.2012.04.002.

Gallovič, František and Lubica Valentová (Feb. 2020). "Earthquake Stress Drops From Dynamic Rupture Simulations Constrained by Observed Ground Motions". en. In: *Geophysical Research Letters* 47.4. DOI: 10.1029/2019gl085880. URL: http://dx.doi.org/10.1029/2019GL085880.

Gallovič, František et al. (2019a). "Bayesian Dynamic Finite-Fault Inversion: 1. Method and Synthetic Test". en. In: *Journal of Geophysical Research: Solid Earth* 124.7, pp. 6949–6969. DOI: 10.1029/2019jb017510. URL: http://dx.doi.org/10.1029/2019JB017510.

Gallovič, František et al. (2019b). “Bayesian Dynamic Finite-Fault Inversion: 2. Application to the 2016 Mw 6.2 Amatrice, Italy, Earthquake”. en. In: *Journal of Geophysical Research: Solid Earth* 124.7, pp. 6970–6988. DOI: 10.1029/2019jb017512. URL: http://dx.doi.org/10.1029/2019JB017512.

Gallovič, František et al. (Oct. 2020). “Complex rupture dynamics on an immature fault during the 2020 Mw 6.8 Elazığ earthquake, Turkey”. en. In: *Communications Earth amp; Environment* 1.1. DOI: 10.1038/s43247-020-00038-x. URL: http://dx.doi.org/10.1038/s43247-020-00038-x.

Graves, Robert W. (Aug. 1996). “Simulating seismic wave propagation in 3D elastic media using staggered-grid finite differences”. en. In: *Bulletin of the Seismological Society of America* 86.4, pp. 1091–1106. DOI: 10.1785/bssa0860041091. URL: http://dx.doi.org/10.1785/BSSA0860041091.

Gutscher and Lallemand (Oct. 1999). “Birth of a major strike-slip fault in SW Japan”. en. In: *Terra Nova* 11.5, pp. 203–209. DOI: 10.1046/j.1365-3121.1999.00247.x. URL: http://dx.doi.org/10.1046/j.1365-3121.1999.00247.x.

Harris, D. (1990). *XAPiir: A recursive digital filtering package*. DOI: 10.2172/6416972. URL: http://dx.doi.org/10.2172/6416972.

Harris, Ruth A. et al. (Apr. 2018). “A Suite of Exercises for Verifying Dynamic Earthquake Rupture Codes”. en. In: *Seismological Research Letters* 89.3, pp. 1146–1162. DOI: 10.1785/0220170222. URL: http://dx.doi.org/10.1785/0220170222.

Hronek, Martin (2023). *Simulace zemětřesení Tottori (Mw 6.1) z r. 2016 pomocí dynamického modelu zdroje*. Bakalářská práce. Praha.

Hutko, Alexander R. et al. (Apr. 2017). “Data Products at the IRIS-DMC: Growth and Usage”. en. In: *Seismological Research Letters* 88.3, pp. 892–903. DOI: 10.1785/0220160190. URL: http://dx.doi.org/10.1785/0220160190.

Ida, Yoshiaki (1972). “Cohesive force across the tip of a longitudinal-shear crack and Griffith’s specific surface energy”. en. In: *Journal of Geophysical Research* 77.20, pp. 3796–3805. DOI: 10.1029/jb077i020p03796. URL: http://dx.doi.org/10.1029/JB077i020p03796.

IRIS (Incorporated Research Institutions for Seismology) (2025). *Radiated energy estimates from the IRIS Earthquake Browser*. Accessed: 2025-03-29. URL: https://ds.iris.edu/ieb/.

Kanamori, Hiroo and Luis Rivera (2006). *Energy partitioning during an earthquake*. DOI: 10.1029/170gm03. URL: http://dx.doi.org/10.1029/170GM03.

Koketsu, K., H. Miyake, et al. (2012). “An updated integrated velocity structure model of Japan based on recent geological and geophysical observations”. In: *Journal of Disaster Research*. URL: https://www.iitk.ac.in/nicee/publications.

Koketsu, K., H. Miyake, Y. Tanaka, et al. (2008). “Development of a 3D velocity structure model for the Kanto Basin for prediction of strong ground motion”. In: URL: https://www.awa.tohoku.ac.jp/publications/2008-kanto-velocity-model.pdf.

Komatitsch, Dimitri et al. (Dec. 2023). *SPECFEM/specfem3d: SPECFEM3D v4.1.0*. Zenodo. DOI: 10.5281/ZENODO.10413988. URL: https://zenodo.org/doi/10.5281/zenodo.10413988.

Kostka, Filip et al. (2021). "Assessing the role of selected constraints in Bayesian dynamic source inversion: application to the 2017Mw 6.3 Lesvos earthquake". en. In: *Geophysical Journal International* 228.1, pp. 711–727. DOI: 10.1093/gji/ggab359. URL: http://dx.doi.org/10.1093/gji/ggab359.

Kristek, Jozef, Peter Moczo, and Martin Galis (Oct. 2009). "A brief summary of some PML formulations and discretizations for the velocity-stress equation of seismic motion". en. In: *Studia Geophysica et Geodaetica* 53.4, pp. 459–474. DOI: 10.1007/s11200-009-0034-6. URL: http://dx.doi.org/10.1007/s11200-009-0034-6.

Kubo, Hisahiko et al. (2017). "Source rupture process of the 2016 central Tottori, Japan, earthquake (M JMA 6.6) inferred from strong motion waveforms". en. In: *Earth, Planets and Space* 69.1. DOI: 10.1186/s40623-017-0714-3. URL: http://dx.doi.org/10.1186/s40623-017-0714-3.

Liu, Jihong et al. (Nov. 2019). "Complete Three-Dimensional Coseismic Deformation Field of the 2016 Central Tottori Earthquake by Integrating Left- and Right-Looking InSAR Observations With the Improved SM-VCE Method". en. In: *Journal of Geophysical Research: Solid Earth* 124.11, pp. 12099–12115. DOI: 10.1029/2018jb017159. URL: http://dx.doi.org/10.1029/2018JB017159.

Madariaga, R., K. Olsen, and R. Archuleta (Oct. 1998). "Modeling dynamic rupture in a 3D earthquake fault model". en. In: *Bulletin of the Seismological Society of America* 88.5, pp. 1182–1197. DOI: 10.1785/bssa0880051182. URL: http://dx.doi.org/10.1785/BSSA0880051182.

Mai, P. Martin et al. (Apr. 2016). "The Earthquake-Source Inversion Validation (SIV) Project". en. In: *Seismological Research Letters* 87.3, pp. 690–708. DOI: 10.1785/0220150231. URL: http://dx.doi.org/10.1785/0220150231.

Meneses-Gutierrez, Angela, Takuya Nishimura, and Manabu Hashimoto (Feb. 2019). "Coseismic and Postseismic Deformation of the 2016 Central Tottori Earthquake and its Slip Model". en. In: *Journal of Geophysical Research: Solid Earth* 124.2, pp. 2202–2217. DOI: 10.1029/2018jb016105. URL: http://dx.doi.org/10.1029/2018JB016105.

Metropolis, Nicholas et al. (1953). "Equation of State Calculations by Fast Computing Machines". en. In: *The Journal of Chemical Physics* 21.6, pp. 1087–1092. DOI: 10.1063/1.1699114. URL: http://dx.doi.org/10.1063/1.1699114.

Moczo, P. et al. (Apr. 2007). "The finite-difference and finite-element modeling of seismic wave propagation and earthquake motion". In: *Acta Physica Slovaca. Reviews and Tutorials* 57.2. DOI: 10.2478/v10155-010-0084-x. URL: http://dx.doi.org/10.2478/v10155-010-0084-x.

Nishimura, Takuya and Youichiro Takada (2017). "San-in shear zone in southwest Japan, revealed by GNSS observations". en. In: *Earth, Planets and Space* 69.1. DOI: 10.1186/s40623-017-0673-8. URL: http://dx.doi.org/10.1186/s40623-017-0673-8.

Okada, Yoshimitsu (Aug. 1985). "Surface deformation due to shear and tensile faults in a half-space". en. In: *Bulletin of the Seismological Society of America* 75.4, pp. 1135–1154. DOI: 10.1785/bssa0750041135. URL: http://dx.doi.org/10.1785/BSSA0750041135.

Petersson, N. Anders et al. (2023). *geodynamics/sw4: SW4, version 3.0*. Zenodo. DOI: 10.5281/ZENODO.8322590. URL: https://zenodo.org/record/8322590.

Premus, Jan, František Gallovič, and Jean-Paul Ampuero (2022). "Bridging time scales of faulting: From coseismic to postseismic slip of the M w 6.0 2014 South Napa, California earthquake". en. In: *Science Advances* 8.38. DOI: 10.1126/sciadv.abq2536. URL: http://dx.doi.org/10.1126/sciadv.abq2536.

Premus, Jan et al. (2020). "FD3D_TSN: A Fast and Simple Code for Dynamic Rupture Simulations with GPU Acceleration". en. In: *Seismological Research Letters* 91.5, pp. 2881–2889. DOI: 10.1785/0220190374. URL: http://dx.doi.org/10.1785/0220190374.

Reuters (Oct. 2016). *Magnitude 6.6 quake jolts western Japan, no tsunami warning or major damage*. Accessed: 2025-06-18. URL: https://www.reuters.com/article/business/environment/magnitude-66-quake-jolts-western-japan-no-tsunami-warning-or-major-damage-idUSKCN12L0F2/.

Ripperger, J. et al. (Apr. 2007). "Earthquake source characteristics from dynamic rupture with constrained stochastic fault stress". en. In: *Journal of Geophysical Research: Solid Earth* 112.B4. DOI: 10.1029/2006jb004515. URL: http://dx.doi.org/10.1029/2006JB004515.

Ross, Zachary E. et al. (Feb. 2018). "Dissipative Intraplate Faulting During the 2016 Mw6.2 Tottori, Japan Earthquake". en. In: *Journal of Geophysical Research: Solid Earth* 123.2, pp. 1631–1642. DOI: 10.1002/2017jb015077. URL: http://dx.doi.org/10.1002/2017JB015077.

Roten, Daniel et al. (Nov. 2016). *High-Frequency Nonlinear Earthquake Simulations on Petascale Heterogeneous Supercomputers*. DOI: 10.1109/sc.2016.81. URL: http://dx.doi.org/10.1109/SC.2016.81.

Sambridge, Malcolm (Oct. 2013). "A Parallel Tempering algorithm for probabilistic sampling and multimodal optimization". en. In: *Geophysical Journal International* 196.1, pp. 357–374. DOI: 10.1093/gji/ggt342. URL: http://dx.doi.org/10.1093/gji/ggt342.

Sambridge, Malcolm and Klaus Mosegaard (2002). "MONTE CARLO METHODS IN GEOPHYSICAL INVERSE PROBLEMS". en. In: *Reviews of Geophysics* 40.3. DOI: 10.1029/2000rg000089. URL: http://dx.doi.org/10.1029/2000RG000089.

Schliwa, Nico et al. (Apr. 2024). *The linked complexity of coseismic and postseismic faulting revealed by seismo-geodetic dynamic inversion of the 2004 Parkfield earthquake*. DOI: 10.31223/x5ft47. URL: http://dx.doi.org/10.31223/X5FT47.

Shibata, Ritsuya and Naofumi Aso (Feb. 2025). "Kinematic Source Modeling Using Radiation-Corrected Empirical Green's Functions in Waveform Inversion". en. In: *Bulletin of the Seismological Society of America* 115.3, pp. 1212–1232. DOI: 10.1785/0120240077. URL: http://dx.doi.org/10.1785/0120240077.

Somerville, Paul (Feb. 2021). "Scaling relations between seismic moment and rupture area of earthquakes in stable continental regions". en. In: *Earthquake Spectra* 37.1$_s$*uppl*, pp. 1534–1549. DOI: 10.1177/8755293020988024. URL: http://dx.doi.org/10.1177/8755293020988024.

Stein, Seth and Michael Wysession (2003). *An Introduction to Seismology, Earthquakes, and Earth Structure*. Malden, MA: Blackwell Publishing. ISBN: 978-0865420786.

Tarantola, Albert (Jan. 2005). *Inverse Problem Theory and Methods for Model Parameter Estimation*. en. DOI: 10.1137/1.9780898717921. URL: http://dx.doi.org/10.1137/1.9780898717921.

U.S. Geological Survey (2025). *USGS Earthquake Catalog*. Accessed: 2025-03-29. URL: https://earthquake.usgs.gov/earthquakes/search/.

Uphoff, Carsten et al. (May 2024). *SeisSol*. Zenodo. DOI: 10.5281/ZENODO.11405512. URL: https://zenodo.org/doi/10.5281/zenodo.11405512.

Wackerly, Dennis, William Mendenhall, and Richard L. Scheaffer (2008). *Mathematical Statistics with Applications*. 7th ed. Belmont, CA: Cengage Learning. ISBN: 978-0495110811.

Zhang, Zhenguo, Wei Zhang, and Xiaofei Chen (2014). "Three-dimensional curved grid finite-difference modelling for non-planar rupture dynamics". en. In: *Geophysical Journal International* 199.2, pp. 860–879. DOI: 10.1093/gji/ggu308. URL: http://dx.doi.org/10.1093/gji/ggu308.